# Chapter 4
# Modelling of Experimental Infections


This chapter aims to give a clear idea of how mathematical analysis for experimental systems could help in the process of data assimilation, parameter estimation and hypothesis testing. In particular, we illustrate the potential of a question-, and data-driven mathematical modelling in the

- estimation of model parameters for the 'virus–host' system,
- understanding kinetic regulation of virus infection dynamics,
- prediction of various phenotypes of virus infections and antigen-specific immune responses,
- testing specific hypothesis about the feedback regulation of T-cell responses.

The material of this chapter is based on our previous work published in [1–4, 9, 51, 84].

## 4.1 Why Experimental Infections?

Experimental systems of various types are used in fundamental immunology to unravel the complex cellular interactions of the immune responses. In vivo systems, which involve the whole animal provides the most natural experimental conditions. However, the in vivo systems have many unknown and uncontrollable interactions that add ambiguity to the interpretation of empirical data. The study of the immune system in vertebrates requires a suitable animal model. For most basic research in immunology, mice have been the experimental animal of choice. To control experimental variation caused by differences in the genetic background of experimental animals, immunologists work with inbred or knock-out or knock-in strains that are genetically identical animals produced by inbreeding. Hundreds of different strains of mice are available these days, e.g. CBA, BALB, C57BL/6, etc.

In this chapter, we present examples of mathematical models developed for experimental virus infection systems to answer specific questions concerning the kinetic



G. Bocharov et al., *Mathematical Immunology of Virus Infections*,
https://doi.org/10.1007/978-3-319-72317-4_4

regulation of virus infection dynamics, which are beyond the realm of purely empirical analysis techniques. The role of mathematical modelling in infection immunology can be summarized as follows:

- Descriptive
  - qualitative and quantitative characterization of process dynamics;
- Explanatory
  - interpretation of the experimental observations,
  - understanding the numbers game;
- Predictive
  - testable predictions; suggestion of new experiments,
  - sensitivity performance quantification,
  - hidden effects.

## 4.2 The LCMV System: Gold Standard for Infection Biology[1]

One of the best-studied model systems of viral infections is the lymphocytic choriomeningitis virus (LCMV) infection in mice.

### *4.2.1 Immunobiology of LCMV*

LCMV is an RNA virus of the Arenaviridae family that is non-cytopathic in vivo, i.e. the virus itself does not cause direct damage to cells and tissues. This feature enables relating any damage that appears in the course of an infection to host immune responses against the virus. Another important feature of the LCMV model system is the existence of several well-characterized viral strains that differ in their replicative capacity, host range (cell tropism and mouse strain) and experimental routes of

[1] Material of subsections (4.2.2–4.2.4) uses the results of our studies from Bocharov, Modelling the dynamics of LCMV infection in mice: conventional and exhaustive CTL responses. J. Theor. Biol. 192, 283–308, Copyright © 1998; Ehl et al., The impact of variation in the number of CD8+T-cell precursors on the outcome of virus infection. Cell. Immunol. 189, 67–73, Copyright © 1998; Bocharov et al., Modelling the dynamics of LCMV infection in mice: II. Compartmental structure and immunopathology. J. Theor. Biol. 221, 349–78, Copyright © 2003; Luzyanina et al., Low level viral persistence after infection with LCMV: a quantitative insight through numerical bifurcation analysis. Math. Biosci. 173, 1–23, Copyright © 2001, with permission from Elsevier and the results of the studies from Proc. Natl. Acad. Sci. USA. (PNAS USA), Bocharov et al., Feedback regulation of proliferation vs. differentiation rates explains the dependence of CD4 T-cell expansion on precursor number, 108, 3318–23, Copyright © 2011 with permission from PNAS USA.

infection (intracranial versus intraperitoneal (i.p.) or intravenous (i.v.)) and thus show different infection outcomes. This enables directly linking easily measurable viral dynamic properties to pathogenic consequences and studying the kinetic mechanisms of chronic infections.

With the use of the LCMV infection model system, a large number of conceptual discoveries in immunology have been made, which are as follows:

- back in 1974/75, Zinkernagel and Doherty demonstrated that cytotoxic T-lymphocytes (CTLs) recognize foreign antigens only in the context of proteins of the major histocompatibility complex (MHC) [5, 6]. For this finding of MHC restriction, they were awarded the Nobel Prize in 1996.
- with the help of knockout mice, the mechanism of CTL-mediated destruction of LCMV-infected target cells in vivo was directly linked to perforin, a pore-forming protein contained in granules of this cell type [7, 8].
- fundamental properties of 'memory' of the adaptive immune response have been understood, in particular, the requirements for CTL memory to prevent the establishment of a persistent LCMV infection [9].
- NK cells of the innate immune response have been recognized as an important regulator of the helper T-cell support for antiviral CTL [10].
- a critical role of organized secondary lymphoid organs in the induction of naive T and B cells and subsequent virus control was established [11].
- the concept of immunopathology, that is the damage of tissues and organs due to the antiviral immune response rather than the infecting virus itself, was established. Mediators of immunopathology include CTL, macrophages, neutrophils and interferons [12–14].
- based on the amino acid similarities between viral antigens and host proteins, the so-called molecular mimicry, viral infections can trigger autoimmunity and influence the course of subsequent infections with other viral pathogens [15–17].
- important observations towards an acute versus a persistent infection outcomes were made as shown in Fig. 4.1 [18–21].

Which infection fate is followed depends on the infecting viral dose and the viral strain and thus can be easily directed experimentally. LCMV persistence is associated with CTL exhaustion, a reversible, non-functional state of CTL. CTL exhaustion is a physiological consequence of persistent antigen exposure and has been observed both in persistent human viral infections and in cancers, the LCMV system was instrumental to understand infection fate regulation in general terms. As CTL exhaustion can be reversed by antibodies against PD1 or PD-L1 that block the negative signalling pathway, novel immunotherapeutic modalities arose which show exciting promises as antiviral and anticancer therapies [22–24].

The LCMV infection model system offers sufficient experimental data to develop mathematical models in a problem-oriented manner. The mathematical model-driven studies of LCMV resulted in experimentally testable predictions concerning the mechanisms of the infection control, for example (i) threshold numbers of initial specific CTL precursors to protect from a chronic LCMV infection outcome, (ii) minimal number of antigen-presenting DCs in spleen for robust induction of CTL

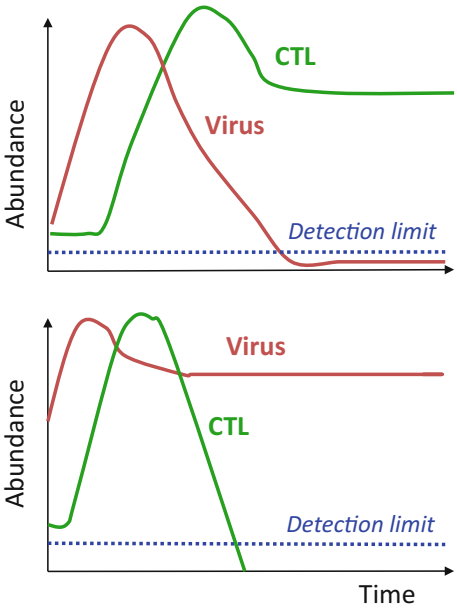


**Fig. 4.1** Scheme of acute (top) and chronic (bottom) LCMV infection. Phenotypically different dynamic patterns of viral load and CTL activity are shown

responses, and (iii) the effect of virus growth rate on the magnitude of the clonal expansion of CTLs, to name just the major of them.

The basic biological features of LCMV, relevant to the mathematical models presented below can be summarized as follows:

- Family: Arenaviridae;
- Strains: Docile, Traub, WE, Aggressive, Armstrong, Clone 13;
- Host: mice, hamsters; humans: acute hemorrhagic fever;
- Target cells: macrophages and lymphocytes;
- Cytopathicity in vivo: non-cytopathic;
- CTL responses play a dominant role in virus clearance: appear early and are high;
- Neutralizing antibody responses: appear only late after infection;
- Immunopathology is a recovery fee: is observed in spleen, liver, central nervous system.

The spatial distribution (compartmental structure) of LCMV infection is presented in Fig. 4.2. It must be noted that spleen plays a central role in LCMV infection as it is a target organ for virus replication and the lymphoid organ in which the antiviral immune response takes place.

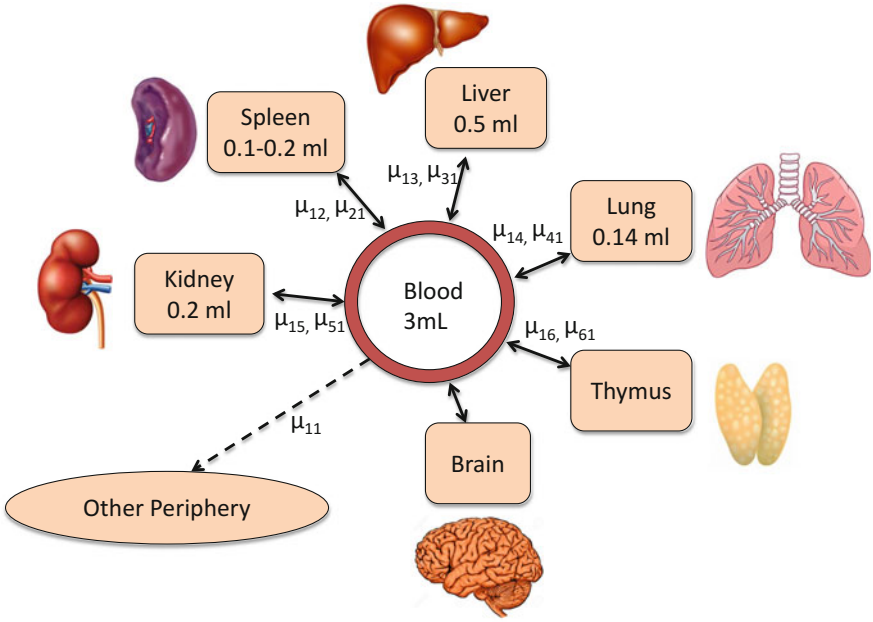


**Fig. 4.2** Scheme of the compartmental structure of LCMV infection spreading in mice. The volumes of the organs, considered as well-mixed reactors, are indicated

### *4.2.2 Basic Mathematical Model of LCMV Infection*

The biological scheme underlying the mathematical model of LCMV infection is presented in Fig. 4.3. The mathematical model of antiviral CTL response developed previously [1] is based upon assumptions reflecting general mechanisms of the virus–host interaction: (i) virus-specific CTLs are primarily responsible for control of infection with non-cytopathic viruses; (ii) the virus population stimulates clonal expansion and differentiation of the specific CTL precursors (CTLp) into effector cells; (iii) a high viral load leads eventually to inhibition of CTL responses via anergy and activation-induced cell death by apoptosis; (iv) in the absence of viral antigens the homeostasis of naive CTLs reflects a balance between the input of the precursor CTLs from thymus and their death at the periphery; (v) virus replication in the host exhibits a logistic-type growth, whereas the elimination follows a second-order kinetics. Only one organ in which both the virus infection and immune response take place (compartment), i.e. the spleen is considered in the basic model. The time-dependent variables of the model are as follows:

- $V(t)$ virus titer in spleen at time $t$ (pfu/ml);
- $E_p(t)$ number of virus-specific precursor CTLs in spleen at time $t$ (cell/ml);
- $E(t)$ number of virus-specific effector CTLs in spleen at time $t$ (cell/ml);
- $W(t)$ cumulative virus antigen load in spleen at time $t$ (pfu/ml).

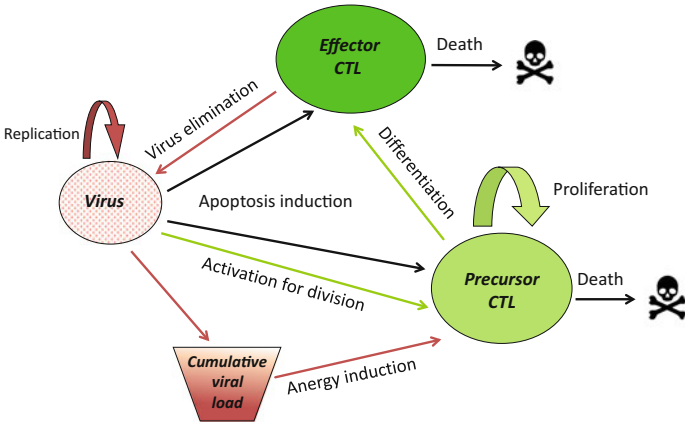


**Fig. 4.3** Schematic representation of the variables and processes considered in the mathematical model of LCMV infection in mice

Their choice is guided by the availability of data for model identification [25] and a clearly elaborated understanding of the most relevant processes in the control of acute LCMV infection. The above-listed processes define the structure of a system of delay differential equations describing the rates of change of the population densities in the course of infection:

$$\frac{dV}{dt} = \beta V(t)(1 - V(t)/K) - \gamma_{VE} V(t) E(t), \tag{4.1}$$

$$\frac{dE_p}{dt} = \alpha_{E_p}\left(E_p^0 - E_p(t)\right) + b_p g_p(W) V(t-\tau) E_p(t-\tau) - \alpha_{AP} V(t-\tau_A) V(t) E_p(t), \tag{4.2}$$

$$\frac{dE_e}{dt} = b_e g_e(W) V(t-\tau) E_p(t-\tau) - \alpha_{AE} V(t-\tau_A) V(t) E_e(t) - \alpha_{E_e} E_e(t), \tag{4.3}$$

$$\frac{dW}{dt} = b_W V(t) - \alpha W(t), \tag{4.4}$$

where $g_p(W) = \frac{1}{(1+W/\theta_p)^2}$, $g_e(W) = \frac{1}{(1+W/\theta_e)^2}$. The equations are supplemented by initial data reflecting the low-, intermediate- and high-dose infections of C57BL/6 mice with LCMV-Docile i.v.:

- $V(t) = 0,\ t \in [-\tau^*, 0),\ V(0) = 10^2,\ 10^4,\ 10^7$ pfu/ml, $\tau^* = \max[\tau, \tau_A]$,
- $E_p(t) = 265$ cell/ml, $t \in [-\tau^*, 0]$,
- $E_e(0) = 0$ cell/ml,
- $W(0) = 0$ pfu/ml.

In the equation for $V(t)$, the first term on the right-hand side describes the virus growth with an upper limit $K$ due to the limited amount of sensitive tissue cells

supporting virus replication, and the second term takes into account the clearance of viruses due to lysis of virus-infected cells by effector CTLs.

In the equation for $E_p(t)$, the first term describes the maintenance of virus-specific precursor CTL at a certain level through their export from thymus and death in the periphery. The second term accounts for an increase in the number of CTL precursors resulting from virus-induced proliferation with the inhibitory effect of cumulative virus load on clonal expansion. The last term describes activation-induced cell death by apoptosis.

The dynamics of $E_e(t)$ is determined by the appearance of mature effector CTLs due to the division and differentiation of antigen-stimulated precursor CTLs with the downregulation of the differentiation process of CTLp due to high virus antigen load (the first term); the decrease in the number of effector CTLs as a consequence of lytic interactions with virus-infected target cells (the second term); the activation-induced cell death of effector CTLs and natural death of effector CTL due to their finite lifespan (two last terms).

In the equation for $W(t)$, the first term describes the increase in the total viral antigen load due to virus spread in the host and the second one accounts for the decrease of the inhibitory effect of high virus loads on the virus-specific CTLs as the virus is eliminated.

The model is based upon a fundamental assumption which reflects results of empirical analysis [25] that continuous exposure of virus-specific CTLs to LCMV induces a sequence of proliferation, anergy and activation-induced cell death by apoptosis. The balance between the above processes depends on the cumulative viral load and shifts towards the anergy and death phenotype in a high viral load infection.

This low-dimensional model is based on (i) a Verhulst logistic form for virus growth; (ii) second-order virus elimination kinetics by CTLs; (iii) the Holling type II response curve for CTLs expansion with a time lag representing cell division time and antigen-independent production/death of CTLs in the immune system (homeostasis).

The relevant information about the model parameters is summarized in Table 4.1.

The model parameters were estimated via a maximum likelihood approach using experimental data characterizing the virus-CTL dynamics after low-, intermediate- and high-dose i.v. infections of C57BL/6 mice [1, 25] and permit a good consistency of the model with the data, Fig. 4.4. The phenomenology of conventional and exhaustive CTL responses is quantitatively captured in the mathematical model.

The phenomenon of exhaustion in the model is defined as disappearance of CTL activity and the functional impairment of virus-specific CTLs. The exhaustion of antiviral CTL responses is modelled as a stepwise process observed in an overwhelming infection with LCMV-Docile. Following the initial activation, LCMV-specific T cells become anergic for 3–5 days and then disappear because of activation-induced cell death (apoptosis). (Of note, the observed lack of T-cell functionality was in time of the described experiments termed anergy; however, this functional state of T cells has been studied in more detail and shown to be a non-responsive state after continuous antigen exposure that is now termed exhausted; for a detailed discussion, see Wherry and Kurachi [26]).

**Table 4.1** The LCMV infection model parameters and their best-fit estimates. We considered one $pfu$ is one infectious $particle$

| Parameter | Biological meaning | Units | Best-fit estimate |
|---|---|---|---|
| $\beta$ | Replication rate constant of viruses | 1/day | 3.35 |
| $\gamma_{VE}$ | Rate constant of virus clearance due to effector CTLs | ml/(cell day) | $1.34 \times 10^{-6}$ |
| $K$ | Virus carrying capacity of spleen | particles/ml | $4.82 \times 10^{7}$ |
| $\tau$ | Duration of CTL division cycle | day | 0.6 |
| $b_p$ | Rate constant of precursor CTL stimulation | ml/(particle day) | $7.73 \times 10^{-5}$ |
| $b_e$ | Rate constant of precursor CTL stimulation | ml/(particle day) | $7.73 \times 10^{-4}$ |
| $\theta_p$ | Cumulative viral load threshold for anergy induction in precursor CTL | particle/ml | $3.25 \times 10^{6}$ |
| $\theta_e$ | Cumulative viral load threshold for anergy induction in differentiation of CTL | particle/ml | $3 \times 10^{5}$ |
| $\alpha_{E_p}$ | Rate constant of precursor CTL natural death | 1/day | 0.542 |
| $\alpha_{E_e}$ | Rate constant of effector CTL natural death | 1/day | 0.01 |
| $E_p^0$ | Homeostatic concentration of LCMV-specific precursor CTL in spleen of unprimed mice | cell/day | 265 |
| $\tau_{AP}$ | Duration of commitment of CTLs for apoptosis | day | 5.6 |
| $\alpha_{AP}$ | Rate constant of precursor CTL apoptosis | $(\text{ml/particle})^2$/day | $7.5 \times 10^{-16}$ |
| $\alpha_{EP}$ | Rate constant of effector CTL apoptosis | $(\text{ml/particle})^2$/day | $4.36 \times 10^{-14}$ |
| $b_W$ | Rate constant of the cumulative viral load growth | 1/day | 1 |
| $\alpha_W$ | Rate constant of the restoration from the inhibitory effect of cumulative viral load | 1/day | 0.11 |

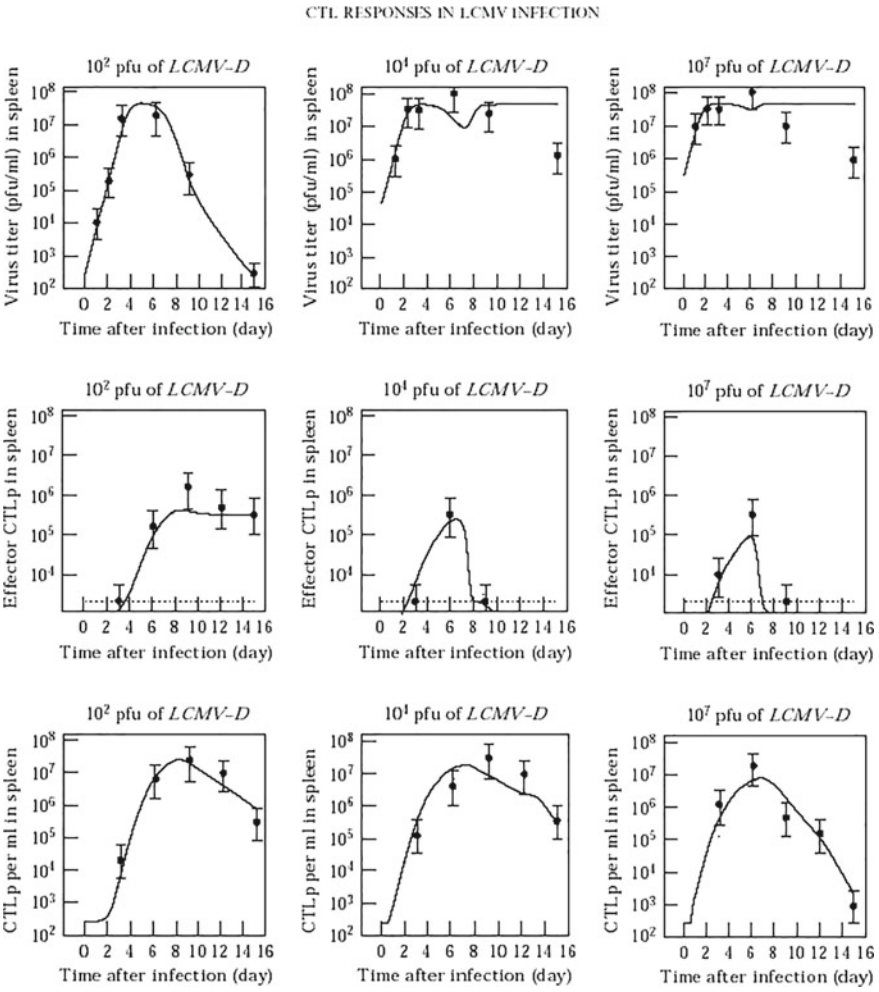


**Fig. 4.4** Solutions of model (4.1–4.4) with the parameters estimated to best-fit the low-, intermediate- and high-dose i.v. infections (Table 4.1). Experimental data are denoted by ∘. Reprinted from Journal of Theoretical Biology, Vol. 192, Bocharov, Modelling the Dynamics of LCMV Infection in Mice: Conventional and Exhaustive CTL Responses, Pages 283–308, Copyright © 1998 with permission from Elsevier

The single characteristic that appeared to be sufficient to control conventional versus exhaustive responses of CTLs was the cumulative viral load (cvl) since the beginning of the infection. The increase of cvl above a certain threshold value in conjunction with the high viral load in the host for about 5 days results in the shift of the infection phenotype from an acute with recovery to a chronic infection.

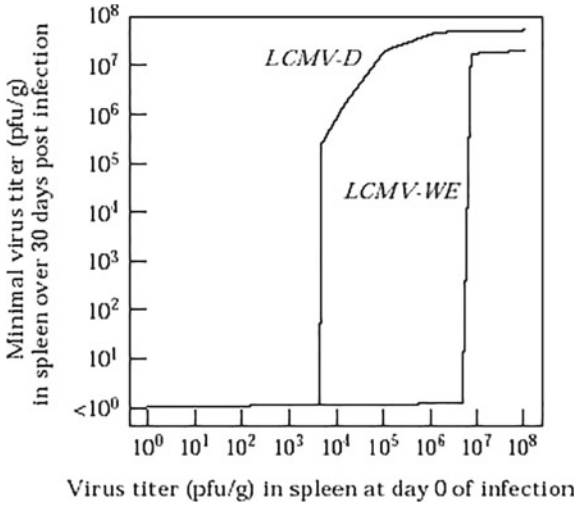


**Fig. 4.5** Model prediction for the dose dependence of virus clearance from the spleen of C57BL/5 mice inoculated i.v. with the indicated doses of LCMV-Docile and LCMV-WE. Reprinted from Journal of Theoretical Biology, Vol. 192, Bocharov, Modelling the Dynamics of LCMV Infection in Mice: Conventional and Exhaustive CTL Responses, Pages 283-308, Copyright © 1998 with permission from Elsevier

### *4.2.3 Viral Parameters: Impact on the Infection Phenotype*

The model predicts that the virus population reaching the spleen after i.v. infection depends on the inoculum size ($IS$) in a nonlinear way, as described by the following formula:

$$V_{Spleen}(day0) = \frac{0.37 \cdot IS}{1 + IS/0.84 \cdot 10^5}. \tag{4.5}$$

It suggests that the fraction of virus population reaching the spleen and establishing a productive infection decreases from 48% to 27% and 0.3% after infection with $10^2$, $10^4$ and $10^7$ pfu, respectively. A continuous dose dependence of the extent of virus elimination from the spleen of infected mice is shown in Fig. 4.5 (left curve). The extent of virus elimination was assessed by the minimal value of the variable $V(t)$ over 30 days post-infection. The extent of virus (LCMV-Docile) clearance displays a threshold-type behaviour in relation to the dose of infection. The doses below $2 \times 10^3$ pfu are eliminated due to the CTL response, while the infections with higher doses lead to CTL exhaustion and virus persistence.

#### 4.2.3.1 Why Does LCMV-WE Strain Fail to Cause Exhaustion of CTLs After i.v. Infection of C57BL/6 Mice?

It is known that some LCMV isolates (WE or Armstrong) do not induce viral persistence after high-dose i.v. infection. However, under certain conditions LCMV-WE can also establish persistent infection like in congenital LCMV-WE carrier C57BL/6 mice. The calibrated model can be used to examine the shape and position of the dose of infection-clearance curve for the LCMV-WE isolate. To this end, using additional

data on the growth kinetics of LCMV-WE, one needs to quantify the exponential growth rate of the virus in spleen and the carrying capacity value. These appear to be smaller than in the cases of LCMV-D, i.e. $\beta = 2.57$ pfu ml$^{-1}$ day$^{-1}$ and $K = 0.18 \times 10^8$ pfu ml$^{-1}$, respectively. Neglecting the differences in CTL stimulation rate due to the variation in amino acids of the LCMV-GP epitope, the infection dose-dependent clearance curve for LCMV-WE can be computed as shown in Fig. 4.5. It suggests that the threshold dose of infection separating clearance and persistence phenotypes is around $7.0 \times 10^6$ pfu. This is an order of magnitude larger than the virus population reaching the spleen after i.v. infection (see 4.5). The difference provides an explanation of why LCMV-WE fails to cause chronic infection after i.v. injection of $10^7$ pfu. Thus, minor variations between the distinct LCMV strains in the values of virus multiplication parameters might underline the about $10^3$ increase in the virus dose threshold separating the two phenotypes of the virus–mouse interaction, i.e. virus clearance and persistent infection.

#### 4.2.3.2 Can Underwhelming Infection Lead to Chronic Persistence?

According to the balance of growth and differentiation concept by Grossman and Paul [80–82], the immune system responds to a strong perturbation of the antigenic homeostasis. The implication is that a slower replicating virus could lead to a weaker immune response. The basic mathematical model of LCMV infection can be used to predict the impact of the virus replication kinetics on the magnitude of the CTL response in acute LCMV infection. To this end, we varied the exponential growth rate of the virus from 1 to 4.8 day$^{-1}$. This corresponds to an increase of the virus population per day by factors of 2.7 and 122. The predicted dependence of the maximum value of $E_p(t) + E_e(t),\ t \in [0, 30]$ days is shown in Fig. 4.6. It appears to be bell shaped.

The experimental analysis of the clonal expansion of CTLs in C57BL/6 mice to LCMV strains (Armstrong, WE-Armstrong, WE, Traub and Docile) differing in their replication rate confirmed that there is a bell-shaped relationship between the LCMV growth rate and the peak CTL response (see Fig. 4.6). Both slow and fast replicating LCMV strains produce weaker CTL responses. Thus, a mechanism of virus persistence by sneaking surveillance due to slow replication kinetics can be hypothesized. The ‘underwhelming’ infection mechanism (supplementing the ‘overwhelming’ infection) fits the above-mentioned concept of the sensitivity of immune responses to perturbations.

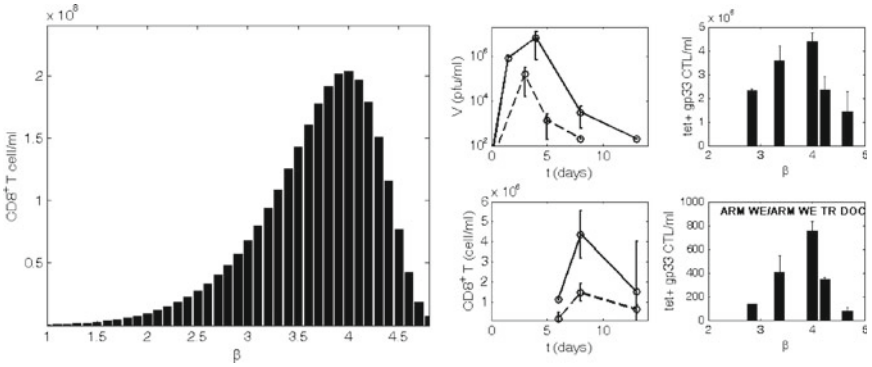


**Fig. 4.6** Dependence of CTL expansion on virus growth rate. Left: Model prediction for i.v. infection with 200 pfu of LCMV stains differing in their replication rates. Center: Data on virus and CTL kinetics for the WE (solid line) and Armstrong (dashed line) strains. Right: Experimental data on the peak CTL responses in blood and spleen for 5 LCMV strains and C57BL/5 mice

#### 4.2.3.3 Low-Level LCMV Persistence[2]

Acute infection with a low-dose LCMV is characterized by virus and CTL dynamics as shown in Fig. 4.7. The viral load drops below the level of detection by conventional assays. Experimental evidence indicates that (i) after acute infection with LCMV the virus might persist for some time in spleen cells at a frequency of 1 copy per $10^4$–$10^5$ splenocytes, giving an estimate of about 500–5000 DNA copies per spleen; (ii) a difference in total LCMV RNA copies between the peak of infection ($10^8 - 10^9$ copies per spleen) and the memory phase ($10^3$ or fewer copies per spleen) has been observed; (iii) infectious LCMV may persist at no more than 100 pfu per spleen [27] and in some cases at the level of 1000 pfu per kidney [28].

How can the virus population persist in the face of CTL memory? There is a diverse array of biological mechanisms that are used by viruses to escape complete elimination by the immune system, ranging from those based on a limited growth, cell-to-cell passage without maturation, localization in an immunologically privileged site, integration into the host cell chromosome to those based on decreasing immune detection and destruction, e.g. via downregulation of MHC-restricted antigen presentation [29–31]. In terms of kinetics, the implication is that the replication rate and CTL-mediated elimination rate of LCMV (represented by $\beta$ and $\gamma_{VE}$, respectively) might well be reduced during transition from the acute to the low-level persistence phase. Indeed, available data on the growth kinetics of LCMV after immune therapy of a persistent viral infection [32] or in $CD4^+$ T cell or B-cell-deficient mice [33] show a much lower rate of viral growth compared to the acute infection.

[2]The material of this subsection uses the results from Luzyanina et al., Low level viral persistence after infection with LCMV: a quantitative insight through numerical bifurcation analysis. Math. Biosci. 173, 1–23, Copyright © 2001, with permission from Elsevier.

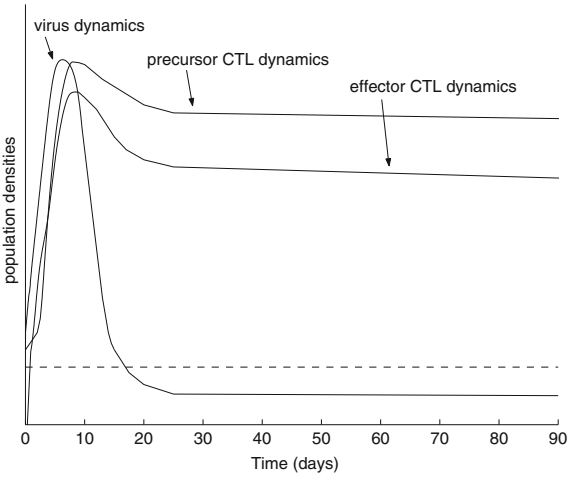


**Fig. 4.7** Scheme of the within-host dynamics of virus and CTL populations characterized by expansion-, contraction- and memory phases. Reprinted from Mathematical Biosciences, Vol. 173, Luzyanina et al., Low level viral persistence after infection with LCMV: a quantitative insight through numerical bifurcation analysis, Pages 1–23, Copyright © 2001, with permission from Elsevier

One can investigate coexistence of viral and CTL populations in the memory phase through numerical bifurcation analysis of the virus–host interaction model.

$$\begin{cases} \frac{\mathrm{d}}{\mathrm{d}t}V(t) = \beta V(t)(1-\frac{V(t)}{K}) - \gamma_{VE}E_e(t)V(t), \\ \frac{\mathrm{d}}{\mathrm{d}t}E_p(t) = \alpha_{E_p}(E_p^0 - E_p(t)) + \frac{b_p}{(1+W(t)/\theta_p)^2}V(t-\tau)E_p(t-\tau) - \alpha_{AP}V(t-\tau_A)V(t)E_p(t), \\ \frac{\mathrm{d}}{\mathrm{d}t}E_e(t) = \frac{b_d}{(1+W(t)/\theta_E)^2}V(t-\tau)E_p(t-\tau) - b_{EV}V(t)E_e(t) - \alpha_{AE}V(t-\tau_A)V(t)E_e(t) \\ \qquad\qquad -\alpha_{E_e}E_e(t), \\ \frac{\mathrm{d}}{\mathrm{d}t}W(t) = b_W V(t) - \alpha_W W(t). \end{cases} \tag{4.6}$$

In the context of dynamical system analysis, the coexistence of a low-level virus population and CTL memory corresponds to a stable steady-state solution (equilibrium) or to a stable oscillatory solution of the model (4.6) with $V$, respectively $V(t)$, below a (small) value, e.g. below the detection level of the virus in experiments. Concerning oscillatory solutions, we are interested in periodic solutions, i.e. solutions both existing in the long term and repeating themselves after a finite time.

For the model analysis, we use the software package DDE-BIFTOOL [34, 35]. DDE-BIFTOOL is a MATLAB package (The MathWorks, Inc.) for bifurcation analysis of systems of DDEs with several discrete delays. The package can be used to compute and analyse the stability of steady-state and periodic solutions of a given system as well as to study the dependence of these solutions on system parameters via continuation.

#### 4.2.3.4 Steady-State Solutions

Introduce the notation $S := [V,\ E_p,\ E_e,\ W]^T$ for a vector of solutions of Eq. (4.6) and $F := F(S(t),\ S(t-\tau),\ S(t-\tau_A),\ p)$ for a vector defined by the right-hand

sides of (4.6) with $p$ a vector of parameters. A steady-state solution, $S^*$, of (4.6) is a solution of the following nonlinear algebraic system,

$$\begin{cases} \beta V(1-\frac{V}{K}) - \gamma_{VE} E_e V = 0, \\ \alpha_{E_p}(E_p^0 - E_p) + \frac{b_p}{(1+W/\theta_p)^2} V E_p - \alpha_{AP} V^2 E_p = 0, \\ \frac{b_d}{(1+W/\theta_E)^2} V E_p - b_{EV} V E_e - \alpha_{AE} V^2 E_e - \alpha_{E_e} E_e = 0, \\ b_W V - \alpha_W W = 0. \end{cases} \tag{4.7}$$

This system is solved by a Newton iteration starting from an initial guess for $S^*$.

The linearization of (4.6) around a solution trajectory $S^*(t)$ is the variational equation,

$$\frac{\mathrm{d}}{\mathrm{d}t} y(t) = A_0(t)y(t) + A_1(t)y(t-\tau) + A_2(t)y(t-\tau_A), \tag{4.8}$$

where $A_i$ equals the derivative of $F$ with respect to its $(i+1)$-th argument evaluated at $S^*(t)$.

For a steady-state solution, $S^*(t) \equiv S^*$, the matrices $A_i(t)$ are constant, $A_i(t) \equiv A_i$, and the variational equation (4.8) leads to a characteristic equation,

$$\det(\lambda I - A_0 - A_1 e^{-\lambda\tau} - A_2 e^{-\lambda\tau_A}) = 0, \tag{4.9}$$

with $I$ the identity matrix. The characteristic roots, $\lambda \in \mathbb{C}$, determine the stability of the steady-state solution $S^*$. In general, (4.9) has an infinite number of roots. However, it is known that $\Re(\lambda_j) \to -\infty$ as $j \to \infty$ and that the number of roots in any right half- plane $\Re(\lambda) > \eta$, $\eta \in \mathbb{R}$, is finite. Hence, the stability is always determined by a finite number of roots. The rightmost (stability determining) characteristic roots are approximated using a linear multi-step method applied to variational equation (4.8), see [34–36] for details. A steplength heuristic is implemented to ensure accurate approximations of the roots with real part greater than a given constant. The approximations thus obtained are corrected using a Newton iteration on the characteristic equation.

Dependence of the steady-state solution $S^*$ on a physical parameter (a component of $p$) can be studied by computing a branch of steady-state solutions as a function of the parameter using a continuation procedure [34]. The stability of the steady state can change during continuation whenever characteristic roots cross the imaginary axis. Generically a *fold* bifurcation (or *turning point*) occurs when a real characteristic root passes through zero and a *Hopf* bifurcation occurs when a pair of complex conjugate characteristic roots crosses the imaginary axis. Once a Hopf point is detected it can be followed in a two-parameter space using an appropriate determining system [34]. In this away, for instance one computes the stability region of the steady-state solution in the two-parameter space (if no other bifurcations occur in this region).

The relevant parameters of virus and CTL memory persistence are those characterizing virus replication and precursor-, effector CTL lifespans: $\beta$, $\alpha_{E_p}$, and $\alpha_{E_e}$.

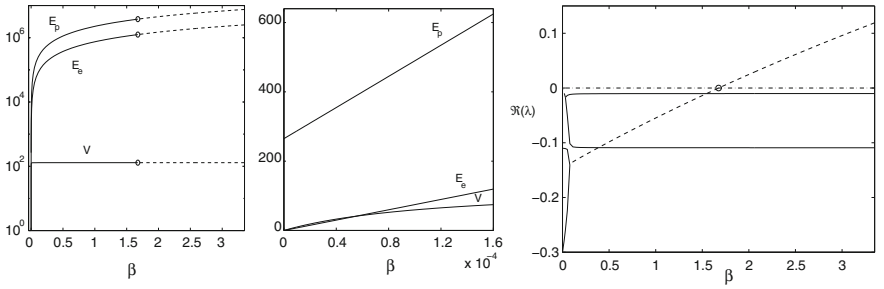


**Fig. 4.8** Left, middle: Solutions $V$ (pfu/ml), $E_p$ (cell/ml) and $E_e$ (cell/ml) along a branch of steady-state solutions of (4.6) versus parameter $\beta$ for $\alpha_{E_e} = 0.3$, $\alpha_{E_p} = 0.01$. Middle figure is a blow up of the left figure. Stable and unstable parts of the branch are denoted by solid, respectively dashed lines. A logarithmic scale is used for the $Y-$axis (Left figure). Right: Real part of the rightmost roots (real $(-)$ and complex $(--)$ roots) of the characteristic equation along the same branch. Hopf bifurcation $(\circ)$ at $\beta \approx 1.675$

We choose the Hopf bifurcation point indicated in Fig. 4.8, as a starting point to continue a branch of Hopf bifurcation points in the $(\beta, \alpha_{E_p})$-plane, see Fig. 4.9 (left). The corresponding Hopf curve bounds the stability region of the steady state corresponding to virus population–CTL memory coexistence because no other bifurcations were found in this region. Using a sequence of similar continuations, we computed branches of Hopf points in the $(\beta, \alpha_{E_p})$-plane for different values of $\alpha_{E_e}$, see Fig. 4.9 (right). Whenever $\alpha_{E_p} < 0.9\alpha_{E_e}$, it can be shown that the numerically established stability regions in the three- parameter space can be approximated by the formula,

$$\beta < 1.7 - 1.8\alpha_{E_p}/\alpha_{E_e}, \tag{4.10}$$

quantitatively describing the nature of the coupling between the parameters necessary to ensure a stable steady state with viral persistence and CTL memory. It indicates an opposite effect of parameters $\alpha_{E_p}$ and $\alpha_{E_e}$ on the value of $\beta$.

Some information about the numerical values of virus and CTL population densities for the steady states in the stability region shown in Fig. 4.9 (left) is given in Fig. 4.10. Figure 4.10 (left) presents the regions in the $(\beta, \alpha_{E_p})$-plane where virus persists below the detection limit ($V < 1000$ pfu/ml) and below 100 pfu/ml. One can see that the value of $V$ almost does not depend on $\beta$ unless $\beta$ gets close to 0 (see also Fig. 4.8) and virus can persist at a very low level if the death rate of CTLp ($\alpha_{E_p}$) is small enough.

#### 4.2.3.5 Periodic Solutions

A periodic solution $S^*(t)$ is a solution which repeats itself after a finite period $T$, i.e. $S^*(t+T) = S^*(t)$ for all $t > 0$. A discrete approximation to a periodic solution on a mesh in $[0, T]$ and its period are computed as solutions of the corresponding

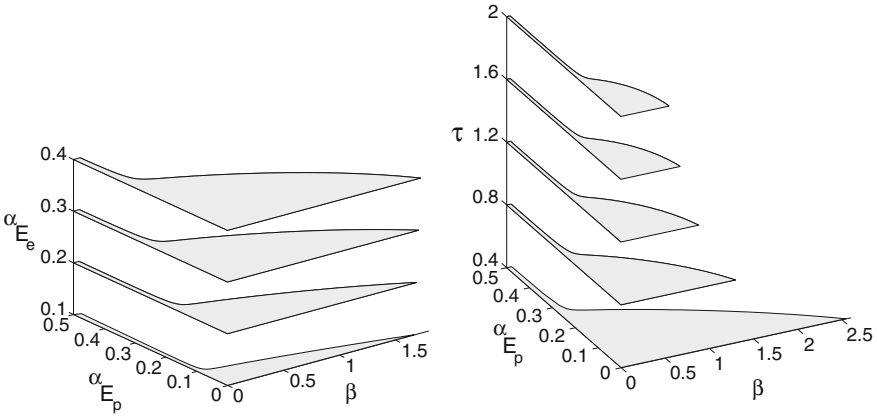


**Fig. 4.9** Stability regions (depicted in grey) of the steady- state solution of (4.6) in the $(\beta, \alpha_{E_p}, \alpha_{E_e})$-space (left) and in the $(\beta, \alpha_{E_p}, \tau)$-space (right). Stability regions are visualized for Left: $\tau = 0.6$; Right: $\alpha_{E_e} = 0.3$. Solid lines correspond to curves of Hopf bifurcations. Reprinted from Mathematical Biosciences, Vol. 173, Luzyanina et al., Low level viral persistence after infection with LCMV: a quantitative insight through numerical bifurcation analysis, Pages 1–23, Copyright © 2001, with permission from Elsevier

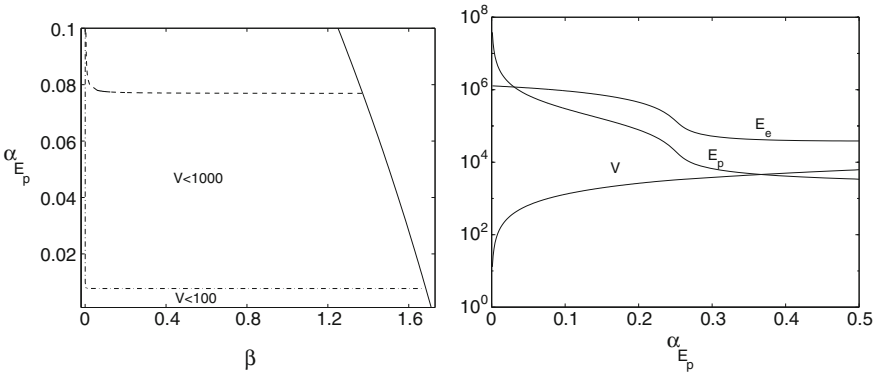


**Fig. 4.10** Left: Regions in the $(\beta, \alpha_{E_p})$-plane corresponding to solutions with $V < 1000$ pfu/ml and $V < 100$ pfu/ml. The solid line denotes a Hopf bifurcation curve. Right: Steady-state solutions $V$ (pfu/ml), $E_p$ (cell/ml), $E_e$ (cell/ml) along the Hopf curve shown in Fig. 4.9 (left). Reprinted from Mathematical Biosciences, Vol. 173, Luzyanina et al., Low level viral persistence after infection with LCMV: a quantitative insight through numerical bifurcation analysis, Pages 1–23, Copyright © 2001, with permission from Elsevier

periodic boundary value problem using piecewise polynomial collocation [37, 38]. Adaptive mesh selection (the lengths of the mesh subintervals are adapted to the solution gradient) allows the computation of solutions with steep gradients.

Stability of a periodic solution is determined by the spectrum of the linear so-called Monodromy operator, which integrates the variational equation (4.8) around $S^*(t)$ from time $t = 0$ over the period $T$. Any nonzero eigenvalue $\mu$ of this operator is called a characteristic (Floquet) multiplier. Furthermore, $\mu = 1$ is always an eigenvalue and it is referred to as the trivial Floquet multiplier. A discrete approximation of this operator, a matrix $M$, is obtained using the collocation equations. The eigenvalues of $M$ form approximations to the Floquet multipliers.

A branch of periodic solutions can be traced as a function of a system parameter using a continuation procedure [34]. The branch can be started from a Hopf point or from an initial guess (e.g. resulting from time integration). Bifurcations of periodic solutions occur when Floquet multipliers move into or out of the unit circle. Generically this is a *turning* point when a real multiplier crosses through 1, a *period doubling* point when a real multiplier crosses through $-1$ and a *torus* bifurcation when a complex pair of multipliers crosses the unit circle.

In the neighbourhood of a Hopf bifurcation point, solutions which belong to a branch of periodic solutions emanating from this point oscillate around the steady-state value corresponding to the Hopf point. Hence, Hopf points with low values of $V$ can be sources of periodic solutions with oscillatory low-level viral persistence. We use the Hopf point shown in Fig. 4.8 as our 'basic Hopf point' and study the existence of oscillatory patterns in viral persistence by computing branches of periodic solutions emanating from this point as a function of the parameters listed in Table 4.1. Note that we depict periodic solutions on the time interval [0, 1], i.e. after time is scaled by the factor $T^{-1}$ with $T$ the period of the solution.

*Influence of* $\beta$. As $\beta$ grows from its Hopf point value ($\beta \approx 1.675$), the amplitude of oscillations of $V(t)$ grows rapidly, see Fig. 4.11. The sensitivity of the dynamics to changes of $\beta$ is also well characterized by the fact that a subtle change in $\beta$ (from 1.675 to 2.06) leads to 'pulse' oscillations in virus population size, see Fig. 4.11 where solutions are shown for three values of $\beta$: close to the Hopf point (a), when $V_{\max} \approx 10^3$ pfu/ml (b) and when $V_{\max} \approx 2 \cdot 10^3$ pfu/ml (c).

We summarized the bifurcation analysis results for $(\beta, \alpha_{E_p})$ in Fig. 4.12, where the curves of the turning points bound regions with different numbers of (stable and unstable) periodic solutions are shown. Note that left parts of the curves of turning points end at Hopf bifurcation points of steady-state solutions. The dynamic complexity of the system is well characterized by the fact that in region 3 steady-state solutions coexist with periodic solutions and in region 2 two stable periodic solutions coexist. However, the region of our interest, where periodic oscillations are such that $V_{\max} < 10^3$ pfu/ml, is quite small. Much smaller is the region with $V$ varying in between 10 and $10^3$ pfu/ml (or equivalently in between 1 and 100 pfu/spleen), see Fig. 4.12 (right). In this region, the period of oscillations varies from 10 to 20 days.

*Influence of* $b_p$. Larger values of $b_p$ increase the region in the $(\beta, \alpha_{E_p})$-plane where oscillatory solutions with $V_{\max} < 10^3$ pfu/ml exist, see region $A$ in Fig. 4.13. However, due to a high sensitivity of the amplitude of oscillations to changes in

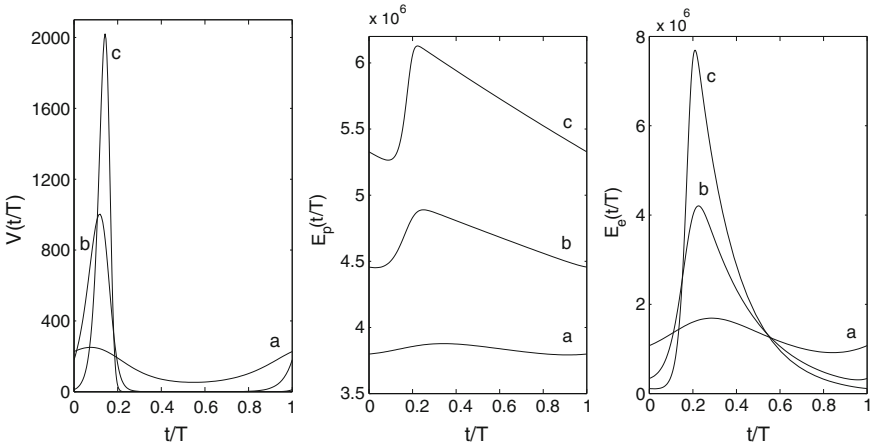


**Fig. 4.11** Sensitivity of periodic solutions to changes in virus growth rate, $\beta$. Solutions $V$ (pfu/ml), $E_p$, and $E_e$ (cell/ml) corresponding to three points on the branch of periodic solutions: $\beta = 1.7$ (**a**), $\beta = 2.06$ (**b**), $\beta = 2.5$ (**c**). Values of the period $T$ (days): $T \approx 9.5$ (**a**), $T \approx 13.2$ (**b**), $T \approx 18.2$ (**c**). Reprinted from Mathematical Biosciences, Vol. 173, Luzyanina et al., Low level viral persistence after infection with LCMV: a quantitative insight through numerical bifurcation analysis, Pages 1–23, Copyright © 2001, with permission from Elsevier

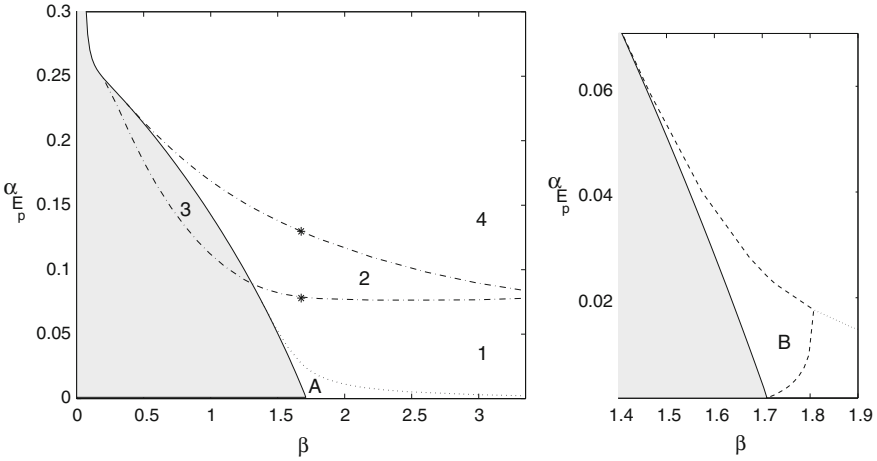


**Fig. 4.12** Left: Stability region (depicted in grey) of the steady-state solution and Hopf curve (solid line) as in Fig. 4.9 (left). Two curves of turning points $(-\cdot)$ of periodic solutions. $(*)$—two turning points corresponding to $\alpha_{E_p} \approx 0.130$, $\alpha_{E_p}$, $\approx 0.078$ (see [2] for further details). Regions of existence of periodic solutions: 1 stable solution (1, 4), 2 stable and 1 unstable solution (2), 1 stable and 1 unstable solutions (3). The dotted line bounds a region ($A$) of existence of periodic solutions with $V_{\max} < 1000$ pfu/ml. Right: A blow up of the left figure. The dashed line bounds a region ($B$) where $V_{\min} > 10$ pfu/ml, i.e. the region with $V$ varying in between 1 and 100 pfu/spleen. $\alpha_{E_e} = 0.3$. Reprinted from Mathematical Biosciences, Vol. 173, Luzyanina et al., Low level viral persistence after infection with LCMV: a quantitative insight through numerical bifurcation analysis, Pages 1–23, Copyright © 2001, with permission from Elsevier

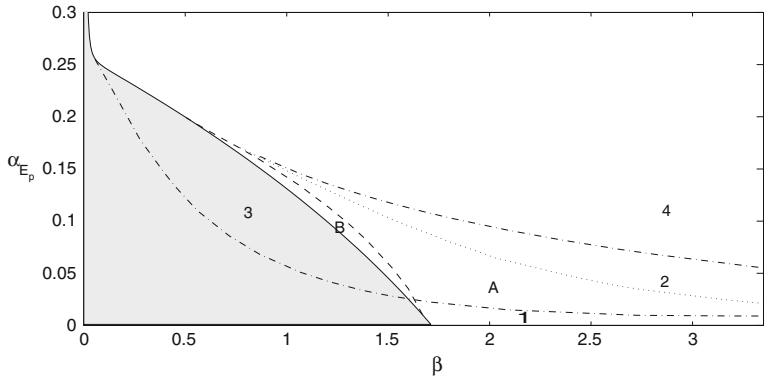


**Fig. 4.13** Stability regions of steady-state- and periodic- solutions for $b_p = 10^{-3}$. All notations are analogous to Fig. 4.12. $\alpha_{E_e} = 0.3$. Reprinted from Mathematical Biosciences, Vol. 173, Luzyanina et al., Low level viral persistence after infection with LCMV: a quantitative insight through numerical bifurcation analysis, Pages 1–23, Copyright © 2001, with permission from Elsevier

values of $\beta$ and $\alpha_{E_p}$ the region where $V_{\min} > 10$ pfu/ml ($B$) remains quite small. Although two stable periodic solutions coexist in a part of region $A$, one of them is not biologically realistic because of very large values of the amplitude and the period of oscillations. Note that the upper left part of region $A$ is bounded by the curve of turning points (which ends at a Hopf point), i.e. for the corresponding values of $\beta$ and $\alpha_{E_p}$ periodic solutions lose stability before $V_{\max}$ reaches $10^3$ pfu/ml.

The effect of other parameters can be briefly summarized as follows.

*Influence of* $\alpha_{E_e}$. As $\alpha_{E_e}$ decreases from 0.3 (Hopf point) to 0.1, the period of oscillations increases to 22 days and $V_{\max}$ increases to 950 pfu/ml. For $\alpha_{E_e} = 0.1$, Hopf bifurcation occurs at $\beta \approx 1.54$, which implies that for $\alpha_{E_e} = 0.1$ the value of $V_{\max}$ grows from 129 to 950 pfu/ml as $\beta$ changes from 1.54 to 1.675. Hence, for $\alpha_{E_e} \in [0.1, 0.4]$ the size of the region in $(\beta, \alpha_{E_p})$-plane where $V_{\max} < 10^3$ pfu/ml is also quite small, and the location of this region with respect to the corresponding Hopf curve is similar to the one shown in Fig. 4.12.

*Influence of* $\tau$. As $\tau$ increases from 0.6 (Hopf point), the amplitude of oscillations grows rapidly and $V_{\max}$ reaches $10^3$ pfu/ml at $\tau \approx 0.8$. At this point the period of oscillations is about 15 days. For $\tau = 0.8$ Hopf bifurcation occurs at $\beta \approx 1.3$, which implies that for $\tau = 0.8$ the value of $V_{\max}$ grows from 129 to $10^3$ pfu/ml as $\beta$ changes from 1.3 to 1.675. Hence for $\tau = 0.8$ the size of the region in $(\beta, \alpha_{E_p})$-plane where $V_{\max} < 10^3$ pfu/ml is also quite small and the location of this region with respect to the corresponding Hopf curve (see Fig. 4.9) is similar to the one shown in Fig. 4.12.

Variations of parameters $b_d$ and $\gamma_{VE}$ within some admissible ranges (see Table 2 in [2] for details) have much lesser impact on the amplitude of oscillations compared to variations of $\beta$, $\alpha_{E_p}$ and $\tau$ and do not change it significantly.

Overall, we found that the periodic solutions with $V$ varying in between 10 and $10^3$ pfu/ml exist in quite narrow intervals of $\beta$ and $\alpha_{E_p}$ values and the amplitude of oscillations grows rapidly as parameters $\beta$, $\alpha_{E_p}$ and $\tau$ increase. So the model predicts

that oscillatory patterns in low level viral persistence (with virus population varying in between 1 and 100 pfu/spleen) are possible for quite 'special' combinations of the rates of virus growth and precursor CTLs death because of a high sensitivity of the amplitude of oscillations to changes in the above parameters.

The main result of our analysis is that unless LCMV replication rate does not reduce to smaller values, as compared to that during the acute phase of primary infection, a low-level persistence in the face of CTL memory as an equilibrium state is not possible: the virus will either be cleared or establishes a high viral load chronic infection, both outcomes depend on the initial dose of infection and the relative kinetics of viral growth. The extent of reduction needed depends on the responder status of the host, in particular, the lifespan of CTL memory subsets, duration of CTL division cycle, activation thresholds of CTL for proliferation, and differentiation. Since the virus remains the same during acute and persistence phase (it should not acquire attenuating mutations) we propose that the reduction in LCMV replication rate resulting in the low-level persistence could be either due to changes in the host cells, e.g. mediated by type I interferons, or intrinsic features of the virus replicatory cycle [39], which slow down the virus growth. This mechanism seems to be in agreement with virus reappearance after in $CD4^+$ T cell help deficient mice, since the deficiency primarily impairs the LCMV-specific $IFN\gamma$ production by CTLs and $CD4^+$ T cells.

### 4.2.4 Role of $CD8^+$ T Cells: Protection, Exhaustion, Immunopathology

LCMV infection of mice is a highly dynamic process with high sensitivity to variation in both host and virus parameters: virus control and functional CTL memory versus virus persistence and complete exhaustion of virus-specific CTL precursors reflect the two extreme ends of this spectrum. While both of these outcomes are of limited pathological consequences for the host, extensive T-cell-mediated immunopathology represents an unfortunate intermediate in the balance of virus–host interactions. Important host and virus parameters that determine the outcome of infection include those controlled by MHC and non-MHC genes, presumably affecting T-cell precursor frequencies and T-cell responsiveness, and virus strain, the route and dose of infection affecting the kinetics of initial virus multiplication and virus distribution. Thus, the susceptibility to the establishment of a virus carrier state is increased with lower CTL responses (low responder status) and slower CTL expansion on the one hand and the ability of the virus to spread rapidly and widely on the other hand.

#### 4.2.4.1 How Many Precursor T Cell are Needed to Protect Against Chronic Infection?[3]

The calibrated mathematical model allows the examination of the effects of variations in virus dose and initial CTLp number on the phenotype of the LCMV infection. Two basic outcomes of the infection can be assessed: virus clearance, i.e. virus titer on day 20 ($V_{min}$) less than the detection limit of 30 pfu per gram of spleen associated with an elevated number of CTLp versus virus persistence ($V_{min} \geq 30$ pfu/g of spleen) and exhaustion of virus-specific CTL.

The impact of variations in the initial number of virus-specific CTLp on control of early virus spread is shown in Fig. 4.14 (left). The effect can also be studied experimentally. To this end C57BL/6 mice were adoptively transfused with $10^7$ spleen virus antigen-specific CTLp from TCR-P14 mice (closed symbols) or left unmanipulated (open symbols). One day later, mice were infected with 500 pfu LCMV-Docile and splenic virus titers were determined daily thereafter in two to three mice per group (Fig. 4.14 centre). The results show that a 1000-fold elevation in the number of CTLp reduces the time until virus clearance was achieved by about 2–3 days. The peak virus concentration reached during the course of the infection is also reduced about 2–3 orders of magnitude. The model and data consistently predict that while further increases in CTLp have an only limited effect, any decrease in the number of CTLp below that of a C57BL/6 mouse results in significant increase in the time until virus elimination is achieved (Fig. 4.14 right).

The model can be further used to predict the impact of variation in the number of virus-specific CTLp on the prevention of virus persistence. The results are sum-

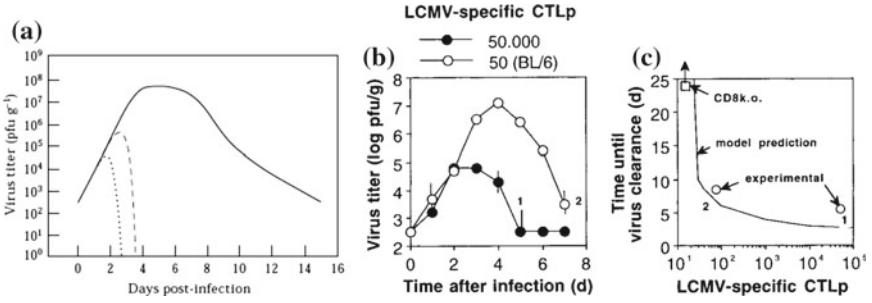


**Fig. 4.14** Impact of variation in the number of virus-specific CTLp on the kinetics of virus clearance. Left: Mathematical model prediction. Centre: Experimental assessment. Right: The relation of the number of initial naive LCMV-specific CTL precursors and the time needed to clear virus from the spleen as predicted by the model and validated experimentally. Reprinted from Cellular Immunology, Vol. 189, Ehl et al., The Impact of Variation in the Number of CD8+T-Cell Precursors on the Outcome of Virus Infection, Pages 67–73, Copyright © 1998, with permission from Elsevier

[3]Material of this subsection uses the results of our studies from Ehl et al., The impact of variation in the number of CD8+T-cell precursors on the outcome of virus infection. Cell. Immunol. 189, 67–73, Copyright © 1998, with permission from Elsevier.

marized in Fig. 4.15, right. In particular, the model predicts that a minimal threshold number of about 25 splenic virus-specific CTLp is needed to prevent virus persistence after infection with 1 pfu. Some of the model-generated predictions were tested experimentally as described below. To address the question of whether and how efficiently an increase in the initial number of virus-specific naive CTL precursors can protect against the establishment of virus persistence, C57BL/6 mice were adoptively transfused with different numbers of spleen cells from TCR-P14 mice such that the splenic CTLp number was varied in the range from 50 to $50 \times 10^3$ cells. One day later, the recipient mice were infected with varying doses of LCMV-Docile i.v. and 20 days after infection, virus titers were determined in the spleen and LCMV-specific CTL activity was assessed after restimulation in vitro. Overall, the following conclusions can be made (see Fig. 4.15, left):

- a minimal threshold number of about 2550 naive LCMV-specific CTL precursors are necessary for control of infections in the range of $1 - 10^4$ pfu;
- with a tenfold higher dose, a 100-fold increase is required to restore virus control;
- in high-dose infection (above $10^6$ pfu), elevations in CTLp were found to be detrimental as they changed the outcome of infection from harmless virus persistence to lethal immunopathology.

In the range where the model predictions could be tested, they were in good agreement with observational data and supported the conclusion that above a certain threshold increases in the number of naive CTLp must be enormous in order to improve virus control. However, the limiting parameter for the efficacy of CTL-mediated virus control is not only the achievement of a critical CTL number in relation to the number of virus-infected cells. Of equal importance is the time required for CTL to mature to be antivirally protective, i.e. the earliest time point when the CTL can efficiently eliminate a population of infected target cells.

The opportunity to compare the model predictions and experimental allows one to define the limitations of the model as a predictive tool related to the fact that it neglected virus spread outside the spleen. While this assumption is presumably justified for low-dose infection, it is responsible for the fact that the model does not account for the significant immunopathology observed after infections with higher doses.

Since the model neglects spread of virus to extralymphatic organs, it is not suited to predict the extent of immunopathology associated with virus clearance from these tissues. The model requires organ-oriented extention to be relevant for examination of the balance between protection and immunopathology by effector memory versus naive precursor CTLs against intravenous or peripheral infections.

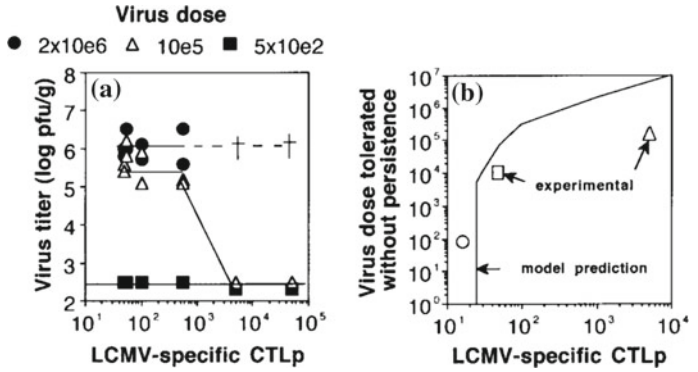


**Fig. 4.15** Impact of variation in the number of virus-specific CTLp on the prevention of virus persistence. Left: Experimental data on splenic virus titers determined in surviving mice 20 days after infection for the indicated doses and initial CTLp number. Right: model prediction on the relation of the number of initial naive LCMV-specific CTL precursors and the maximum dose of virus that can still be eliminated from the spleen within 20 days after infection. Reprinted from Cellular Immunology, Vol. 189, Ehl et al., The Impact of Variation in the Number of CD8+T-Cell Precursors on the Outcome of Virus Infection, Pages 67–73, Copyright © 1998, with permission from Elsevier

### 4.2.4.2 Modelling LCMV-Associated Liver Disease[4]

Infection of mice LCMV represents an example of a systemic infectious process, where the localization, dose and time of availability of virus antigens are important parameters determining the outcome of infection by affecting the antiviral immune response and pathological consequences of the cytotoxic T lymphocyte- (CTL) mediated destruction of virus-infected cells [40, 41]. It provides an experimental model system for studying diseases mediated by cytotoxic activity of effector CTL against cells expressing virus antigen such as diabetes [42, 43], aplastic anemia [44], choriomeningitis [45], liver disease [46], to name just few of them. A classical example is the LCMV-WE-induced liver hepatitis in mice [47].

The problem closely related to systemic virus spread is CTL-mediated immunopathology. This depends on the extent of virus distribution in peripheral tissues as well as the relative kinetics of the CTL response and is an important determinant of the outcome of infection. Virus-induced CTL responses represent heterogeneous populations of cells in different activation and differentiation states: activated cycling, cytolytic effector and quiescent memory cells. These subsets differ essentially in their function and ability to migrate to peripheral sites of infection. Because LCMV is non-cytopathic, virus clearance from the host through CTL-mediated perforin-dependent destruction of infected cells is always associated with a varying degree of immunopathology. Under small infectious doses virus replication

[4]Material of this subsection uses the results of our studies from Bocharov et al., Modelling the dynamics of LCMV infection in mice: II. Compartmental structure and immunopathology. J. Theor. Biol. 221, 349–78, Copyright © 2003, with permission from Elsevier.

is localized mainly to the spleen so that virus-triggered CTL-dependent destruction of infected antigen-presenting cells (macrophages and dendritic cells) is manifested as acquired immune suppression [48, 49]. Large doses of systemic or any peripheral infections lead to a wider spread of the virus in the host and can induce other types of immunopathology, depending on the tissue damage involved (e.g. choriomeningitis). The type of pathology in natural and experimental systems depends on

- the route of infection (intravenous, intracerebral, intrahepatic, etc.),
- tissue tropism of the virus,
- the dose of infection and
- immune status of the host.

All these factors interact nonlinearly to produce various infection outcomes ranging from virus elimination to lifelong persistence. A quantitative characterization and prediction of the outcome of infection in murine LCMV system requires consideration of the three aspects of infection:

1. systemic virus spread,
2. lymphocyte migration during immune responses to tissue sites outside the spleen and
3. the pathological consequences of virus elimination via perforin-dependent CTL-mediated destruction of infected cells.

In this section, we formulate a mathematical model to investigate the demands to CTL memory for protection against LCMV infection with minimal immunopathology. To address the immunopathology question, the basic model of LCMV infection in spleen was extended to consider additional organs, i.e. blood and liver. Such extension should allow to examine the severity of LCMV-associated CTL-induced hepatitis.

Formulation of a multi-compartmental mathematical model integrating the kinetics of LCMV spread in various tissues of mice with effector CTL activation and trafficking allow one to specify the parameters which have to be achieved for CTL vaccination/immunization to ensure virus elimination with minimal immunopathology versus vaccination for disease. To keep the mathematical model in accord with what is experimentally controlled [47], one can consider the dynamics of two enzymes signalling liver cells destruction, $AST(t)$ and $ALT(t)$ as disease characteristics.

The mathematical model for CTL-mediated hepatitis in LCMV infection considers the population dynamics of infection and immune response in three organs (compartments), i.e. the blood, spleen and liver, as shown in Fig. 4.2. The compartmental structure of the model is formulated as a linear mamillary compartmental system [50]:

$$\frac{d}{dt}\mathbf{y}(t) = \mathbf{M} \times \mathbf{y}(t), \tag{4.11}$$

where $\mathbf{y}$(t) is a state vector of spatially distributed species.

The corresponding set of differential equations for LCMV-induced hepatitis considers the population dynamics of

- virus titer in spleen, blood and liver: $V_{Spleen}(t)$, $V_{Blood}(t)$, $V_{Liver}(t)$;

- precursor CTLs in spleen: $E_p(t)$;
- recirculating effector CTLs in spleen, blood and liver: $E_{e,Spleen}(t)$, $E_{e,Blood}(t)$, $E_{e,Liver}(t)$;
- cumulative viral load in spleen: $W(t)$;
- liver enzymes levels in blood: $AST(t)$, $ALT(t)$.

The basic model of LCMV infection in spleen (developed in Sect. 4.2) has to be modified and extended to take into account the virus transfer between blood and spleen as well as the recirculation of effector CTLs between blood and spleen. The procedure is outlined in detail in [51]. Implementing a building block approach, it can be described in the following structured form. *Splenic LCMV infection module*:

$$\left\{\begin{array}{l}
\frac{\mathrm{d}}{\mathrm{d}t}V_{Spleen}(t) = \mu_{SB}V_{Blood}(t) - \mu_{BS}V_{Spleen}(t) \\
\qquad +\beta V_{Spleen}(t)(1-\frac{V_{Spleen}(t)}{V_{mvc,Spleen}}) - \gamma_{VE}E_{e,Spleen}(t)V_{Spleen}(t)/(1+E_{e,Spleen}(t)/\theta_{VE,S}), \\
\frac{\mathrm{d}}{\mathrm{d}t}E_p(t) = \alpha_{E_p}(E_p^0 - E_p(t)) + \frac{b_p}{(1+W(t)/\theta_p)^2(1+(E_p(t)+E_{e,Spleen}(t))/E_{PE}^{Sat})}V_{Spleen}(t-\tau)E_p(t-\tau) \\
\qquad -\alpha_{AP}V_{Spleen}(t-\tau_A)V_{Spleen}(t)E_p(t), \\
\frac{\mathrm{d}}{\mathrm{d}t}E_{e,Spleen}(t) = \eta_{SB}E_{e,Blood}(t) - \eta_{BS}E_{e,Spleen}(t) \\
\qquad +\frac{b_d}{(1+W(t)/\theta_E)^2(1+(E_p(t)+E_{e,Spleen}(t))/E_{PE}^{Sat})}V_{Spleen}(t-\tau)E_p(t-\tau) - b_{EV}V_{Spleen}(t)E_{e,Spleen}(t) \\
\qquad -\alpha_{AE}V_{Spleen}(t-\tau_A)V(t)E_{e,Spleen}(t) - \alpha_{Ee}E_{e,Spleen}(t) \\
\qquad -\alpha_{PCD}/(1+V_{Spleen}(t)/\theta_{PCD})E_{e,Spleen}(t), \\
\frac{\mathrm{d}}{\mathrm{d}t}W(t) = b_W V_{Spleen}(t) - \alpha_W W(t).
\end{array}\right. \tag{4.12}$$

Note that the equation for the effector CTLs in spleen has additional terms which describe saturation of CTL expansion rate at high population densities and passive effector cell death under condition of limiting antigen in the spleen. We assume $b_{EV} = 0$.

Additional equations for virus dynamics in blood and liver are as follows:

$$\left\{\begin{array}{l}
\frac{\mathrm{d}}{\mathrm{d}t}V_{Blood}(t) = \mu_{BS}V_{Spleen}(t) + \mu_{BL}V_{Liver}(t) - (\mu_{SB}+\mu_{LB}+\varepsilon_B)V_{Blood}(t) \\
\frac{\mathrm{d}}{\mathrm{d}t}V_{Liver}(t) = \mu_{LB}V_{Blood}(t) - \mu_{BL}V_{Liver}(t) \\
\qquad +\beta V_{Liver}(t)(1-\frac{V_{Liver}(t)}{V_{mvc,Liver}}) - \gamma_{VE}E_{e,Liver}(t)V_{Liver}(t)/(1+E_{e,Liver}(t)/\theta_{VE,L})
\end{array}\right. \tag{4.13}$$

The module describing the recirculation of effector CTLs between blood and liver is

$$\left\{\begin{array}{l}
\frac{\mathrm{d}}{\mathrm{d}t}E_{e,Blood}(t) = \eta_{BS}E_{e,Spleen}(t) + \eta_{BL}E_{e,Liver}(t) - (\eta_{LB}+\eta_{SB}+\delta_B)E_{e,Blood}(t) \\
\frac{\mathrm{d}}{\mathrm{d}t}E_{e,Liver}(t) = \eta_{LB}E_{e,Blood}(t) - (\eta_{BL}E_{e,Liver}(t) + \delta_L)E_{e,Liver}(t).
\end{array}\right. \tag{4.14}$$

The equations for enzymes dynamics in blood are as follows:

$$\left\{\begin{array}{l}
\frac{\mathrm{d}}{\mathrm{d}t}AST(t) = \rho_{AST}V_{Liver}(t))E_{e,Liver}(t)/(1+E_{e,Liver}(t)/\theta_{VE,L}) \\
\qquad -\alpha_{AST}AST(t) \\
\frac{\mathrm{d}}{\mathrm{d}t}ALT(t) = \rho_{ALT}V_{Liver}(t))E_{e,Liver}(t)/(1+E_{e,Liver}(t)/\theta_{VE,L}) \\
\qquad -\alpha_{ALT}ALT(t).
\end{array}\right. \tag{4.15}$$

The model was calibrated using diverse sets of published data as described in details in [51]. The parameters of the model are listed in Table 4.2.

**Table 4.2** List of the model parameters estimated for systemic LCMV-WE infection in CB57BL/6 mice

| Parameter | Biological meaning | Units | Best-fit estimate |
|---|---|---|---|
| $\beta$ | Replication rate constant of viruses in spleen | 1/day | 4.7 |
| $V_{mvc}$ | Maximal virus concentration in spleen | pfu/ml | $6.5 \times 10^8$ |
| $\beta$ | Replication rate constant of viruses in liver | 1/day | 2.1 |
| $V_{mvc}$ | Maximal virus concentration in spleen | pfu/ml | $3.0 \times 10^8$ |
| $\gamma_{VE}$ | Rate constant of virus clearance due to effector CTLs | ml/(cell day) | $2.5 \times 10^{-5}$ |
| $\theta_{VE}$ | CTL number of half-maximal virus clearance rate | cell/ml | $2.6 \times 10^5$ |
| $E_p^0$ | Homeostatic concentration of LCMV-specific CTLs in spleen of unprimed mouse | cell/ml | 1100 |
| $\alpha_{E_p}$ | Rate constant of natural death for precursor CTLs | 1/day | 0.068 |
| $b_p$ | Rate constant of CTL stimulation | ml/(pfu day) | $2 \times 10^{-3}$ |
| $\tau$ | Duration of CTL division cycles | day | 1.0 |
| $b_d$ | Rate constant of CTL differentiation | ml/(pfu day) | $2 \times 10^{-2}$ |
| $\theta_p$ | Cumulative viral load threshold for anergy induction in precursor CTLs (proliferation process) | pfu/ml | $1 \times 10^6$ |
| $\theta_E$ | Cumulative viral load threshold for anergy induction in effector CTLs (differentiation process) | pfu/ml | $5.5 \times 10^5$ |
| $\alpha_{PCD}$ | Rate constant of effector CTL death after virus clearance below a threshold | l/day | 0.3 |

(continued)

**Table 4.2** (continued)

| Parameter | Biological meaning | Units | Best-fit estimate |
|---|---|---|---|
| $\theta_{PCD}$ | Extent of virus elimination at which the passive cell death is in effect | l/day | 1.0 |
| $\alpha_{E_e}$ | Rate constant of natural death for effector CTLs | pfu/ml | 0.068 |
| $\tau_A$ | Duration of commitment of CTLs for apoptosis | day | 9.1 |
| $\alpha_{AP}$ | Rate constant of apoptosis for precursor CTLs | $(\text{ml/pfu})^2/\text{day}$ | $1.0 \times 10^{-13}$ |
| $\alpha_{AE}$ | Rate constant of apoptosis for effector CTLs | $(\text{ml/pfu})^2/\text{day}$ | $3 \times 10^{-14}$ |
| $b_W$ | Rate constant of viral load increase | 1/day | 1.7 |
| $\alpha_W$ | Rate constant of restoration from the inhibitory effect of virus load | 1/day | 0.4 |
| $E_{EP}^{Sat}$ | Saturation rate constant for CTL expansion | cell/ml | $1.0 \times 10^7$ |
| $\rho_{AST}$ | Rate constant of AST release into blood from CTL destroyed infected liver cell | U/l/(pfu cell day) $\text{ml}^2$ | $1.0 \times 10^{-9}$ |
| $\rho_{ALT}$ | Rate constant of ALT release into blood from CTL destroyed infected liver cell | U/l/(pfu cell day) $\text{ml}^2$ | $0.7 \times 10^{-9}$ |
| $\alpha_{AST}$ | Decay rate of AST in blood | 1/day | 0.5 |
| $\alpha_{ALT}$ | Decay rate of ALT in blood | 1/day | 0.5 |

**Table 4.3** Transfer rates ($hr^{-1}$) of LCMV between Blood-, Spleen- and Liver compartments

| Organ | Blood | Spleen | Liver |
|---|---|---|---|
| Blood | $-0.74$ | $0.33 \times 10^{-3}$ | $0.27 \times 10^{-4}$ |
| Spleen | $0.5 \times 10^{-3}$ | $-0.33 \times 10^{-3}$ | 0 |
| Liver | $0.74 \times 10^{-2}$ | 0 | $-0.27 \times 10^{-4}$ |

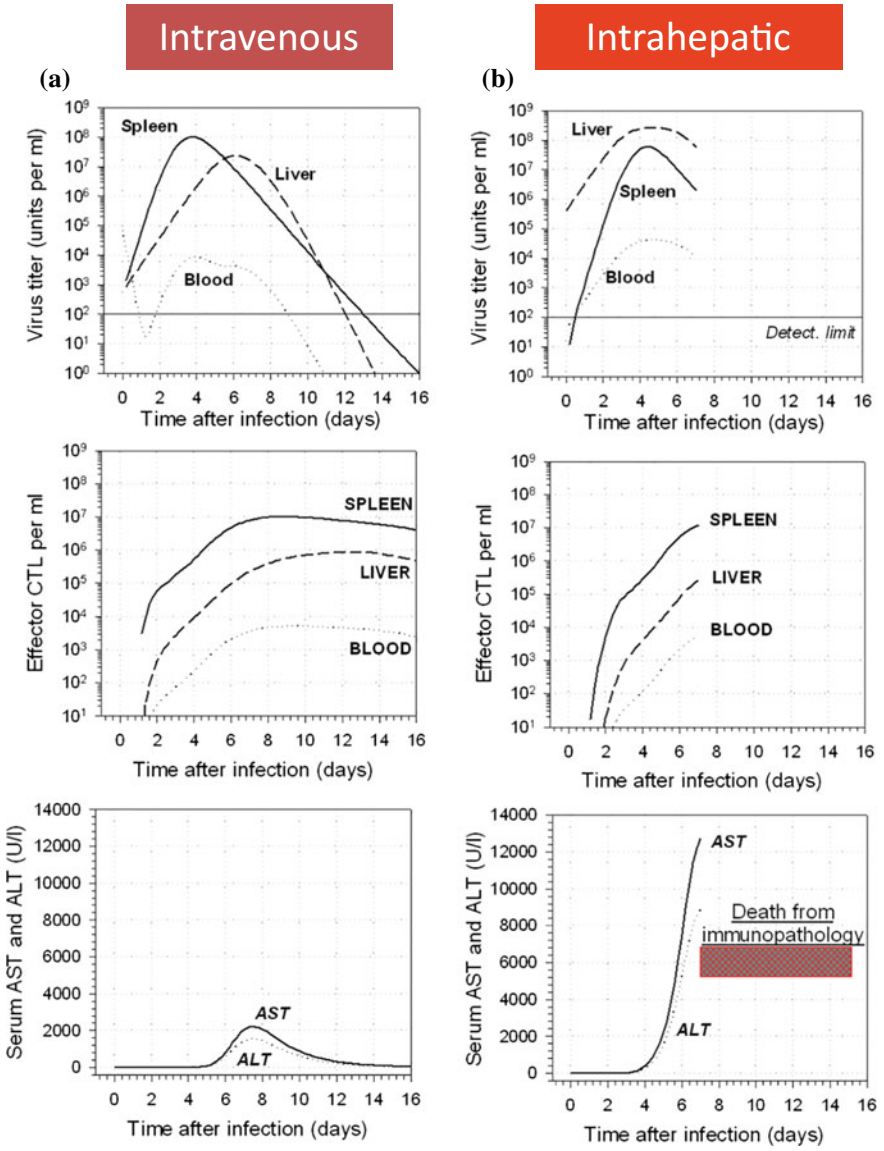


**Fig. 4.16** Model prediction for the dynamics of liver disease associated with LCMV infection of C57BL/6 mice. Two qualitatively different routes of application of $2 \times 10^5$ pfu of LCMV-WE are considered: **a** systemic infection leads to acute infection with modest immunopathology and elimination of the virus; **b** peripheral route of infection via liver leads to severe immunopathology and death of the animal by day 6 post-infection. Reprinted from Journal of Theoretical Biology, Vol. 221, Bocharov et al., Modelling the Dynamics of LCMV Infection in Mice: II. Compartmental Structure and Immunopathology, Pages 349–378, Copyright © 2003, with permission from Elsevier

**Table 4.4** Trafficking rates ($day^{-1}$) of effector CTLs between Blood-, Spleen- and Liver compartments

| Organ | Blood | Spleen | Liver |
|---|---|---|---|
| Blood | −20 | 0.25 | 0.2 |
| Spleen | 10 | −0.25 | 0 |
| Liver | 10 | 0 | −0.2 |

The transfer rates, i.e. the elements of compartmental matrix **M**, for virus and effector CTL are specified in Tables 4.3 and 4.4, respectively.

The example of compartmental dynamics of LCMV infection predicted by the model is shown in Fig. 4.16a. It presents the simulation of the CTL-mediated liver disease after i.v. infection of C57BL/6 mice with $2 \times 10^5$ pfu of LCMV-WE. The model predicts that: (i) virus growth in the liver proceeds at a slower rate than in spleen and the viremia lasts for about 1 week; (ii) CTL response in spleen eliminates the splenic virus in about 10 days starting from day 4; (iii) it takes 3 days more to overcome virus replication in the liver and this time lag is needed for effector CTL to accumulate in liver above the threshold number, estimated to be $1.24 \times 10^5$ cells per ml of liver, for which the basic reproductive ratio of the virus in liver becomes less than one; (iv) the serum enzyme levels start to rise at high rate by day 5 after infection.

The dynamics and outcome of LCMV infection after peripheral route of infection is quite different. In Fig. 4.16b, the simulation of a direct injection of $2 \times 10^5$ pfu of LCMV-WE into the liver of C57BL/6 mouse is shown. The model predicts that virus extensively replicates in liver reaching the maximum possible titer of $3 \times 10^8$ pfu/ml by day 5, which implies that all target cells get infected. Virus growth in the spleen is decreased and delayed by about 1 day as compared to the i.v. infection, and therefore, the splenic CTL response starts later. By day 5, when effector CTLs accumulate in the liver in large number, the destruction of all the infected hepatocytes results in a fulminant immunopathology as is manifested in the model by the enormous elevation of AST and ALT levels. Therefore, this particular combination of viral and host parameters leads to a lethal outcome.

Adoptive transfer experiments demonstrated that virus-specific CTLs are crucial in production of LCMV-associated hepatitis. We examined the 'dose-effect' relationship between the number of effector CTLs injected into blood from one side and the peak serum AST levels and the time until virus in spleen declines below detection limit of 100 pfu/ml on the other side. The scenario of experimental i.v. infection of a naive C57BL/6 mouse with $2 \times 10^5$ pfu of LCMV-WE accompanied with adoptive transfer of effector $CD8^+$ T cells at day 0 was mathematically modelled to determine the maximum serum AST level. The predicted effect of the number of transferred effector CTL and peak AST is shown in Fig. 4.17 Left, (b). It suggests that a higher number of injected effectors decreases the severity of clinical disease, and injection of about $10^3$ cells is enough to reduce the AST level below 500 U/l. The time required

to eliminate virus below detection limit displays a non-monotone pattern, it declines from 14 to 7 days as the number of transferred effector CTL increases from 0 to $10^5$. Further increase of transferred CTL above $4 \times 10^5$ cells leads to a rapid virus elimination within 1 day with no signs of disease. Note, that the narrow suboptimal range of transferred CTL represents the situation when the basic reproductive ration of virus infection is close to 1.

The effect of increase in number of virus-specific precursor CTL in spleen (the responder immune status) on the severity of LCMV-WE- induced liver disease and the time of virus elimination is summarized in Fig. 4.17 Left, (c). A lifelong virus persistence and CTL exhaustion are predicted by the model as an outcome of systemic infection with $2 \times 10^5$ pfu of mice with less than 20 precursor CTLs in spleen. The minimal number of precursor CTL to clear an infection is about 100 per spleen. The time needed for virus elimination decreases with the increase in the number of precursor CTLs but does not go below 4 days, in contrast to the case of effector CTLs. For initial numbers of precursor CTLs in spleen ranging from 30 to 100 cells the outcome of the high-dose infection would be a severe or fatal hepatitis, reflecting an unfavourable combination of viral and host parameters.

The validation of the model was conducted by comparing its predictions on the virus dose dependence of serum enzyme concentration with experimental observations. The results and data available for C57BL/6 and ICR mice, the last one known as being more susceptible to LCMV-WE-induced hepatitis than C57BL/6 mice, are shown in Fig. 4.17a. The data shown are the averages for 2–4 mice bled at the times indicated. The mathematical model based upon data for LCMV-WE infection of C57BL/6 mice predicts a dose-effect curve which is situated below the data for ICR mice. However, it is consistent with three available data points for C57BL/6 mice representing the severity of infection with $2 \times 10^5$ pfu of LCMV-WE. Overall, the model predicts the following functional relationship between the peak AST level in blood and the dose (ranging from 0 to $10^6$ pfu) of i.v. infection:

$$AST_{max} \sim \sqrt{V_{blood}(0)} \tag{4.16}$$

that is the severity of the hepatitis increases as a squared root of the infection dose.

The mathematical model can be further used to examine the infection outcome/severity of the liver disease after peripheral LCMV-WE infection with $2 \times 10^5$ pfu via liver, i.e. intrahepatic infection. The liver infection of naive C57BL/6 mice would result in severe hepatitis for doses ranging in between 10 and $10^6$ pfu, see Fig. 4.17 Right, (a). One might try to prevent this unfavourable outcome by adoptively transferring LCMV-specific effector or precursor CTLs. The impact of effector CTL is presented in Fig. 4.17 Right, (b). First, there exists a threshold number of effector CTL $\sim 2 \times 10^5$ cells conferring an immediate type of protection against virus spread and severe disease. With the CTL number above the threshold, the LCMV population is eliminated in less than 1 day, with no signs of the disease. If the number of transferred lytic CTL is below threshold then protection against the liver disease is not conferred, although the virus is likely to be eliminated.

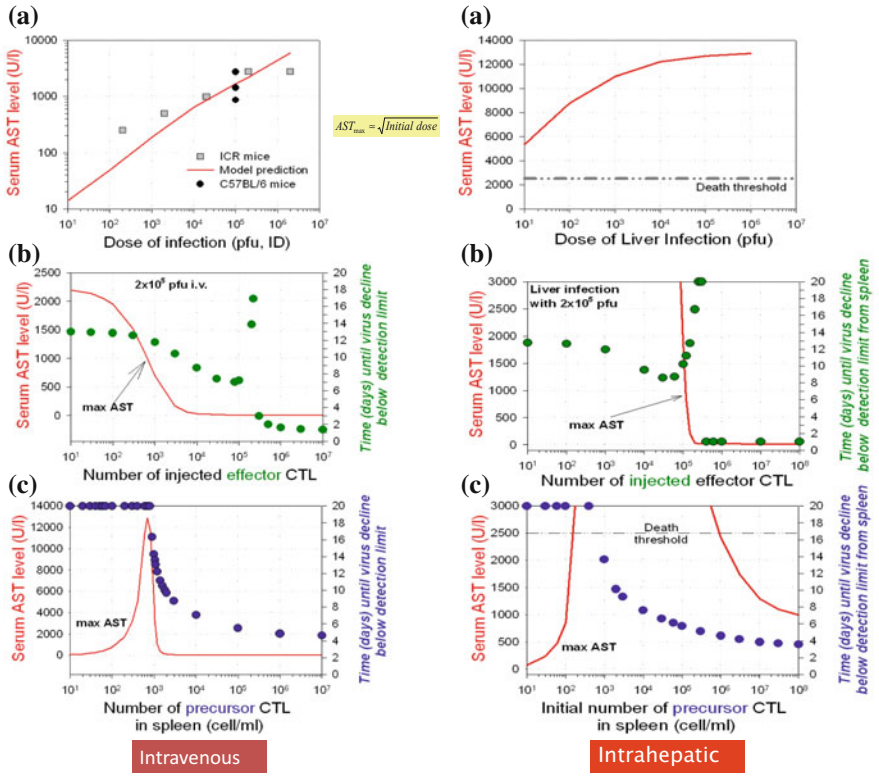


**Fig. 4.17** Analysis of the impact of viral and immune status parameters on the essential characteristics of LCMV-WE infection associated liver disease. Left: Intravenous infection with $2 \times 10^5$ pfu is considered. Left: I.v. infection. **a** severity of the disease in terms of peak AST level as a function of initial virus dose; **b** effect of the initial number of virus-specific cytolytic effector $CD8^+$ T cells injected into blood at day 0 of infection on the serum AST level and the time until virus is eliminated below detection level of 100 pfu/ml; **c** effect of the initial number of precursor $CD8^+$ T cells present in spleen at day 0 of infection on the serum AST level and the time until virus is eliminated below detection level of 100 pfu/ml. Right: Peripheral infection. **a** severity of the disease in terms of peak AST level as a function of initial virus dose; **b** effect of the initial number of virus-specific cytolytic effector $CD8^+$ T cells injected into blood at day 0 of infection on the serum AST level and the time until virus is eliminated below detection level of 100 pfu/ml; **c** effect of the initial number of precursor $CD8^+$ T cells present in spleen at day 0 of infection on the serum AST level and the time until virus is eliminated below detection level of 100 pfu/ml. Reprinted from Journal of Theoretical Biology, Vol. 221, Bocharov et al., Modelling the Dynamics of LCMV Infection in Mice: II. Compartmental Structure and Immunopathology, Pages 349–378, Copyright © 2003, with permission from Elsevier

Figure 4.17 right, (c) predicts the effect of the LCMV-specific precursor CTLs present in the spleen at the moment of infection on the peak AST level and virus elimination time. Low numbers (less than 20 cells per spleen) of CTLp are associated with virus persistence, CTL exhaustion and no symptoms of hepatitis. For the initial

number of CTLp in between 20 and $10^5$ cells a severe or fatal hepatitis would be an outcome of the intrahepatic infection with $2 \times 10^5$ pfu. Only the population of splenic precursor CTLs larger than $10^5$ cells would provide protection against virus persistence, but at the expense of a marked damage of the infected liver. Even with $10^7$ LCMV-specific precursor CTLs in the spleen, the mouse would need at least 4 days to eliminate the virus and the associated immunopathology would still be above 1000 U/l. This time lag is required for them to get activated and generate sufficient number of effector CTLs.

Overall, a 'Complete' characterization of the outcome of virus–host organism interaction with a mathematical model requires consideration of not only the immune response and viral dynamics, but also some characteristics of tissue damage. A new 'spatial' dimension can be introduced into the model via compartmental analysis.

The extended model quantitatively predicts that there is a range for the initial number of precursor CTLs in spleen for which an elevation in the clonal size is accompanied by an increase of disease immunopathology. Thus, it overcomes the predictive limitations of a single-compartmental model as discussed in Sect. 4.2 and reflects what was described experimentally as 'vaccination for disease' [16].

## 4.3 Parameters Defining a Robust DC-Induced CTL Expansion[5]

Successful vaccination depends on the availability of specific antigens, efficient delivery of these antigens, and their optimal presentation to T cells within secondary lymphoid organs. The growing knowledge of the molecular identity of tumour-specific antigens has opened new avenues for effective cancer vaccines [52]. Immunotherapeutic approaches based on adoptive transfer of dendritic cells (DC) expressing relevant antigens may be used for active mobilization of cellular immune responses (CTLs, T-helper cells and NK cells) against tumours. DC-based immunotherapeutic approaches appear particularly promising because DC migrate to the T-cell zones of secondary lymphoid organs where they efficiently initiate both Th and CTL responses [53, 54]. The extraordinary efficacy of DC to prime immune responses is shown by the fact that only $10^2 - 10^3$ antigen-presenting DCs in the spleen are sufficient to achieve protective levels of CTL activation in mice [55]. A series of preclinical experimental studies in mice demonstrated that anti-tumour immunity can be induced using DC [56–59]. This preclinical experience has been translated into the performance of a variety of clinical trials, which have shown that application of DC is safe and that clinical efficacy of this treatment strategy can be obtained [60–62].

The efficacy of this active immunization depends on the complex biology of the DC life cycle and their interaction with T cells. The kinetics of this interaction and its sensitivity to relevant parameters are still incompletely understood. These parameters include antigen loading, DC maturation stage, frequency and route of DC injection,

[5] Material of this section uses the results from Ludewig et al., Eur J Immunol. 34 (2004), 2407–18.

frequency and activation status of T cells, and the homing rate of DC to and their persistence within lymphoid tissues. However, the major quantitative parameters of the DC–CTL interaction (e.g. the elimination kinetics of DC by CTL, the threshold for T cell activation, and the impact of DC on T cell homing and recirculation) require further analysis.

In this section, we present one possible approach to modeling the interaction of DCs with CTLs. In the presented model, the DC–CTL interaction is described by adapting different theoretical frameworks, such as predator–prey models from population biology and Monod-type kinetics with saturation which are applied in biochemistry. We are considering the underlying processes at the macroscopic level of the whole immune system via a compartmental approach and aim to produce a meaningful mathematical model that is both descriptive and predictive. Using a combination of experimental in vivo work and mathematical modelling, we examine here the systemic aspects of DC–CTL interactions. The interdisciplinary approach presented below is composed of three major segments:

1. initial data collection and model establishment by data assimilation;
2. evaluation of effects of varied parameters in a range that is easily accessible to the model prediction but not experimental measurement;
3. model predictions on DC-based immunization and experimental validation.

### *4.3.1 The Experimental Model of LCMV gp33-Specific CTL Induction*

The experimental murine system based on priming of $CD8^+$ T cells specific for the immunodominant gp33-peptide of the lymphocytic choriomeningitis virus (LCMV) glycoprotein presented by DC proved to be valuable in assessing relevant parameters of CTL induction and maintenance [56, 63, 64]. Reliable input from experimental or clinical research in terms of precise and comprehensive data sets is a core part of an interdisciplinary modelling approach. The data set for model-driven analysis was generated using established protocols [55, 63]. Briefly, major histocompatibility complex (MHC) class I tetramers complexed with the immunodominant CTL epitope (gp33) derived from the glycoprotein of the lymphocytic choriomeningitis virus (LCMV-GP) were used to follow activation of gp33-specific CTLs after immunization with DC. DCs derived from transgenic mice ubiquitously expressing the first 60*aa* of LCMV-GP including gp33 (H8-DC) were injected intravenously into naive C57BL/6 recipient mice. At the specific time points following immunization, the densities of the following cell populations as a function of time t were determined:

- Activated $CD8^+$ $62L^-$ T-cells staining with the gp33-tetramer (tet+) in spleen
- Quiescent $CD8^+CD62L^+tet^+$ cells in spleen $E_m(t)$;
- The availability of adoptively transferred DC for productive interaction with T-cells within secondary lymphoid organs was quantified. To this end 51Cr-labelled H8-

DC were injected i.v. into naive recipient mice, and the accumulated radioactivity was determined in spleen at different time points using established protocols [65].

The data set for homing of adoptively transferred DC from blood to spleen has been published elsewhere [84].

### *4.3.2 Mathematical Model for DC-Induced Systemic Dynamics of CTL Responses*

Mathematical models for the interaction of antigen-presenting cells (APC) and T cells developed so far, consider mainly the stimulatory aspects of the interaction of APC and T cells [67, 68]. However, CTL-mediated killing of the antigen-presenting DC is probably a key process in the downregulation of adaptive immune responses [63, 69, 70]. The positive amplification effect of antigen-presenting DC on the CTL population and the negative feedback from CTL on DC numbers implies that the cell population dynamics of the CTL–DC system in vivo most likely reflects a predator–prey type of interaction (Fig. 4.18). Mathematical modelling facilitates the analysis of the following issues: (i) suitability of the predator–prey-type framework for the dynamics of the DC–CTL system in vivo; (ii) estimation of thresholds for DC-mediated CTL induction and trafficking; (iii) analysis of sensitivity of CTL dynamics to various parameters (e.g. half-life of DC and the initial number of precursor T cells); and (iv) role of TCR avidity in the robustness of CTL priming.

To formulate equations for DC–CTL interaction following i.v. injection, we make the following simplifying biological assumptions. Such a list is also helpful for the evaluation of the modelling results from the viewpoint of the underlying biology. A conceptual model for the predator–prey-type induction/regulation of CD8+ T-cell responses by dendritic cells is shown in Fig. 4.18. Antigen-expressing DC migrate from blood to spleen, where they induce clonal expansion of nave antigen-specific cytotoxic T-lymphocytes (CTL), whereas activated CTL eliminates DC. Arrows indicate the modeled processes. The structure of the model equations is based on the following assumptions:[6]

1. DC do not recirculate from lymphoid organs into the blood after intravenous injection.
2. Adoptively transferred DC are in mature state.
3. DC-mediated induction of antigen-specific CTL is due to their interaction in the spleen.
4. DC do not divide in secondary lymphoid organs.
5. DC decay due to a short lifespan and their killing by activated CTL.

[6](see for details Bocharov et al., (2005): A Mathematical Approach for Optimizing Dendritic Cell-Based Immunotherapy. In: *Adoptive Immunotherapy. Methods and Protocols*, Eds. Ludewig B. and Hoffmann M.W. (Humana Press) **109**: 19–34).

6. The population of antigen-specific CTLs in spleen is split into quiescent (nave or central memory-like) and activated CTL (effector or effector memory-like).
7. CTL recirculate among spleen, blood and peripheral organs (e.g. liver).

To formulate the systemic model, we follow a building block approach and calibrate submodels (1) for initial DC distribution, (2) DC–CTL population dynamics in spleen, and (3) the compartmental dynamics of CTL responses.

#### 4.3.2.1 Initial DC Migration

I.v. injection of DCs leads to one way migration to the peripheral organs, i.e. spleen, liver, lung and others. The rate of chage of the DCs population is described by

$$\frac{d}{dt}D_{Blood}(t) = -\left(\mu_{BS} + \mu_{BL} + \mu_{BLu} + \mu_{BO}\right) \cdot D_{Blood}(t) \tag{4.17}$$

$$\frac{d}{dt}D_{Spleen}(t) = \mu_{BS} \cdot D_{Blood}(t)\frac{Q_{Blood}}{Q_{Spleen}} \tag{4.18}$$

$$\frac{d}{dt}D_{Liver}(t) = \mu_{BL} \cdot D_{Blood}(t)\frac{Q_{Blood}}{Q_{Liver}} \tag{4.19}$$

$$\frac{d}{dt}D_{Lung}(t) = \mu_{BLu} \cdot D_{Blood}(t)\frac{Q_{Blood}}{Q_{Lung}} - \mu_{LuO} \cdot D_{Lung}(t) \tag{4.20}$$

The transfer parameters estimated from experimental data are gived in Table 4.5.

#### 4.3.2.2 DC–CTL Interaction in Spleen

The submodel for DC and CTL interaction in spleen reflects a biological view of the processes as depicted in Fig. 4.18.

The rate of change in the density of DC in the spleen is modelled as

**Table 4.5** Transfer rates ($hr^{-1}$) of DC between Blood-, Spleen-, Liver- and Lung compartments

| Organ | Blood | Spleen | Liver | Lung |
|---|---|---|---|---|
| Blood | −1.124 | 0 | 0 | 0 |
| Spleen | 0.12 | 0 | 0 | 0 |
| Liver | 0.38 | 0 | 0 | 0 |
| Lung | 0.16 | 0 | 0 | −0.0911 |

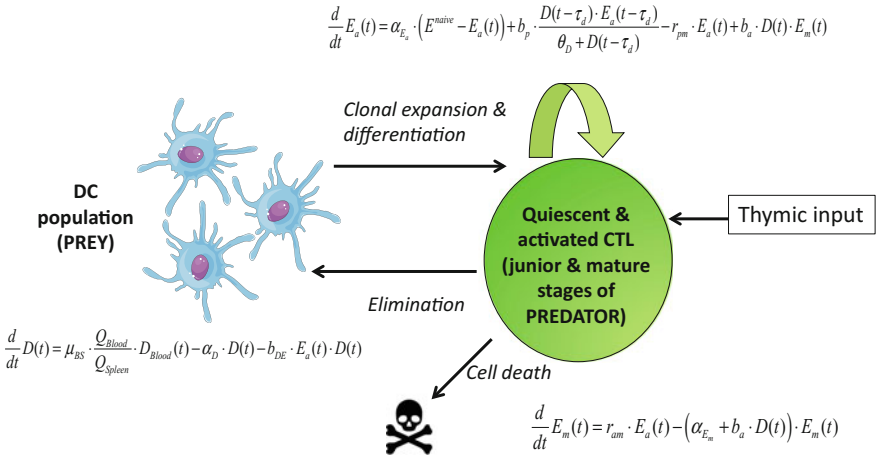


**Fig. 4.18** Scheme of the predator–prey type interaction between CTL responses and DCs in spleen used for the model formulation. Arrows indicate the modelled processes which appear as individual terms on the right-hand sides of specified equations. *Cell Pictures taken from Servier Medical Art*

$$\frac{d}{dt}D(t)=\mu_{BS}\cdot\frac{Q_{Blood}}{Q_{Spleen}}\cdot D_{Blood}(t)-\alpha_D\cdot D(t)-b_{DE}\cdot E_a(t)\cdot D(t). \quad (4.21)$$

The first term represents the trafficking of DCs from blood to spleen ($Q_{Blood}$ and $Q_{Spleen}$ being the volumes of the blood and spleen compartments, respectively), and the other two take into account the natural death of the cells and their elimination by activated CTLs.

The dynamics of activated CTLs is modelled by the following equation:

$$\frac{d}{dt}E_a(t)=\alpha_{E_a}\cdot\left(E^{naive}-E_a(t)\right)+b_p\cdot\frac{D(t-\tau_d)\cdot E_a(t-\tau_d)}{\theta_D+D(t-\tau_d)}-r_{am}\cdot E_a(t)+b_a\cdot D(t)\cdot E_m(t) \quad (4.22)$$

The first term considers the homeostasis of naive CTLs in the spleen, the second term represents the DC-induced division of CTLs proceeding at the rate that saturates at a high number of DCs. The time lag between the cognate interaction of CTL with DC represents the duration of pre-programming of CTL for division and differentiation. The last two terms take into account the silencing of activated CTLs into quiescent memory cells (third term) and the activation of the memory cells by DCs.

The equation for the dynamics of quiescent memory CTLs is

$$\frac{d}{dt}E_m(t)=r_{am}\cdot E_a(t)-\left(\alpha_{E_m}+b_a\cdot D(t)\right)\cdot E_m(t) \quad (4.23)$$

which considers the transition of the activated CTLs into the quiescent memory state, the death of memory CTLs at some slow rate, and the activation of memory CTLs depending on the availability of DCs.

The above model for DC–CTL interaction in the spleen was fitted to the experimental data sets to estimate the parameters via a maximum likelihood approach. We assumed that the observational errors of the data follow a log-normal distribution and are independent between cell populations. The relevant information about the model parameters governing the DC–CTL interaction in the spleen is summarized in Table 4.6. The corresponding solution of the model is shown in Fig. 4.19.

The model predicts that the threshold of DC density for half-maximal CTL expansion rate in the spleen is about 200 cells per spleen which explains the rather small effects in the chosen dose range on the magnitude of the CTL response. The amplification factor of the CTL expansion is about 12 cells per day implying that the pre-programming effect probably lasts for three to four divisions. The estimate of per capita CTL-mediated elimination rate of the DC ($b_{DE}$) suggests that the threshold number of activated CTLs eliminating about 50% of antigen-presenting DCs per day is about $1.4 \times 10^4$ per spleen. Furthermore, the model predicts that about 7% of the activated CTLs enter the memory pool.

#### 4.3.2.3 Compartmental Dynamics of CTL Responses

The next step is to extend the spleen-localized model to the systemic dynamics of a DC-induced CTL response according to the scheme shown in Fig. 4.20. The extended model considers the dynamics of DC–CTL interactions in spleen and CTL recirculation between spleen, blood and liver. The trafficking of both activated and quiescent antigen-specific CTLs between the spleen, blood and liver is described in a uniform way as a nonlinear compartmental system. Using the vector notation for the CTL subsets densities in the above compartments $\mathbf{E}_i(t) = \left[E_i^{Blood}(t), E_i^{Spleen}(t), E_i^{Liver}(t)\right]^T,\ i = a, m$

$$\frac{d}{dt}\mathbf{E}_i(t) = \mathbf{M}^{E_i} \cdot \mathbf{E}_i(t)(t) + \mathbf{I}_i(t), \tag{4.24}$$

where $\mathbf{E}_i(t)$ is a state vector of organ distributed CTLs in activated and memory states. Here the compartmental matrix stands for CTL inter-compartmental transfer rates.

$\mathbf{M}^{E_i} = \begin{pmatrix} -\mu_{BB} & \mu_{SB}(D_{Spleen}(t)) & \mu_{LB} \\ \mu_{BS} & -\mu_{SB}(D_{Spleen}(t)) & 0 \\ \mu_{BL} & 0 & -\mu_{LB} \end{pmatrix}$, with $\mu_{SB}(D_{Spleen}(t)) = \mu_{SB}^* + \frac{\Delta\mu}{1+D_{Spleen}(t)/\theta_{shut}}$.

Here, the DC-dependent migration rate from the spleen to the blood takes into account the trapping effect. The input/output vector-function $\mathbf{I}_i(t) = \left[0, (\text{division} - \text{death})_{Spleen}, 0\right]^T$ represents the contribution of DC-induced CTL responses in the spleen.

The estimated trafficking rate parameters for CTLs are listed in Table 4.7. The computed curves of CTL dynamics versus the experimental data are shown in Fig. 4.21. A critical feature for the systemic response is that CTL transfer rates from spleen to blood appear to be DC-density dependent. To describe the observed CTL

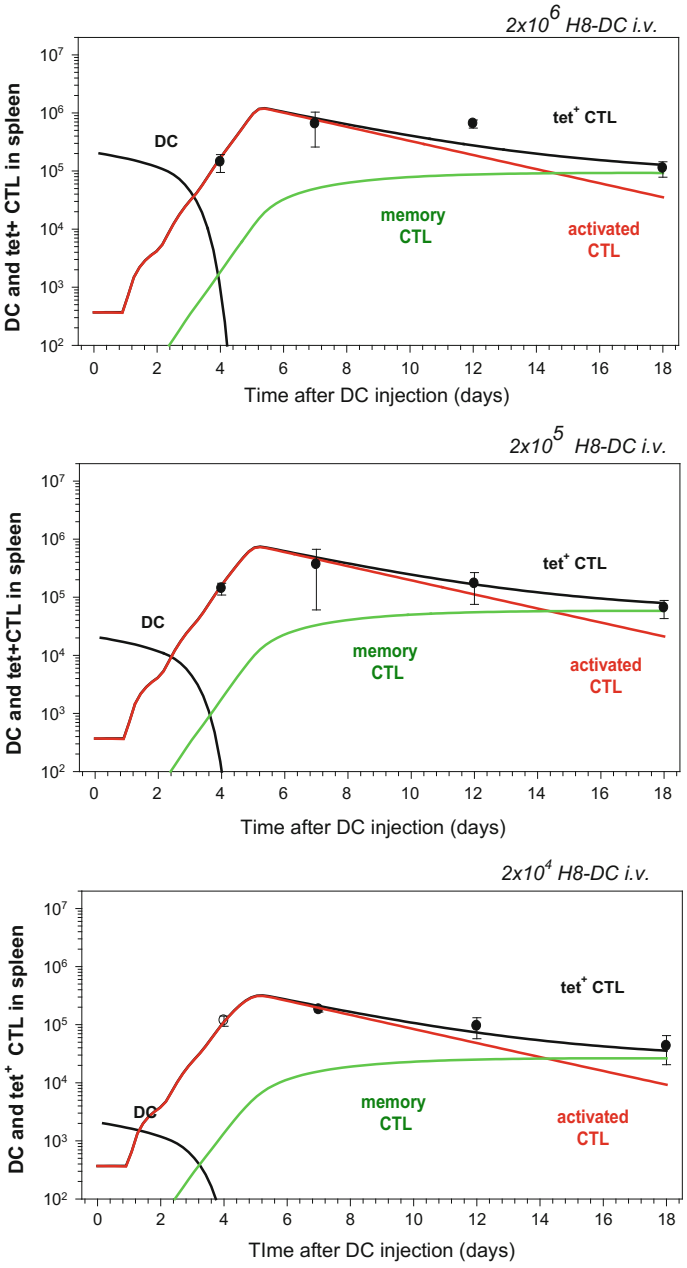


**Fig. 4.19** Data versus model description for the population dynamics of DCs and CTLs in spleen induced by i.v. injection of $2 \times 10^4$, $2 \times 10^5$, $2 \times 10^6$ gp33-presenting H8-DCs. The symbols represent averages of 3 mice $\pm$ SD. The lines describe the predicted populations dynamics of total tet+, activated tet+ and quiescent memory tet+ CTL and H8-DC. DC elimination follows a biphasic kinetics, the first slower phase reflects their life-span and the accelerated decay phase results from the killing effect by activated CTLs. (The figure is adapted from Ludewig et al., EJI, 2004)

**Table 4.6** The estimated parameters of the mathematical model of H8-DC-induced CTL population dynamics

| Parameter | Biological meaning | Units | Best-fit estimate |
|---|---|---|---|
| $\mu_{BS}^{H8-DC}$ | Transfer rate of H8-DCs from blood to spleen | 1/day | 2.832 |
| $\alpha_D$ | Decay rate of gp-33 expressing DCs | 1/day | 0.23 |
| $b_{DE}$ | Per capita elimination rate of H8-DCs by activated CTLs | ml/(cell day) | $0.487 \times 10^{-5}$ |
| $E^{naive}$ | The number of naive gp-33-specific CTLs contributing to primary clonal expansion | cell | 370 |
| $\tau_d$ | Duration of pre-programmed CTL division cycle | day | 1 |
| $\alpha_{E_a}$ | Rate constant of activated CTLs death | 1/day | 0.12 |
| $\alpha_{E_m}$ | Rate constant of resting memory CTLs death | 1/day | 0.01 |
| $b_p$ | Maximal expansion factor of activated CTLs per day | 1/day | 12 |
| $\theta_D$ | Threshold in DC density in the spleen for half-maximal proliferation rate of CTL | cell/ml | $2.12 \times 10^3$ |
| $r_{am}$ | Rate constant of reversion of activated CTLs | 1/day | 0.01 |
| $b_a$ | Activation rate constant of quiescent CTLs by DCs | ml/(cell day) | $1.05 \times 10^{-3}$ |
| $\theta_{shut}$ | Threshold in DC density in the spleen for half-maximal transfer rate of CTL from spleen to blood | cell/ml | 13.0 |

kinetics, one needs to consider the possibility of the DC-dependent retention of T cells. Thus, the model predicts a trapping effect, which reduces the export rate of CTLs to blood by about tenfold above a threshold of about 10 H8-DCs present in

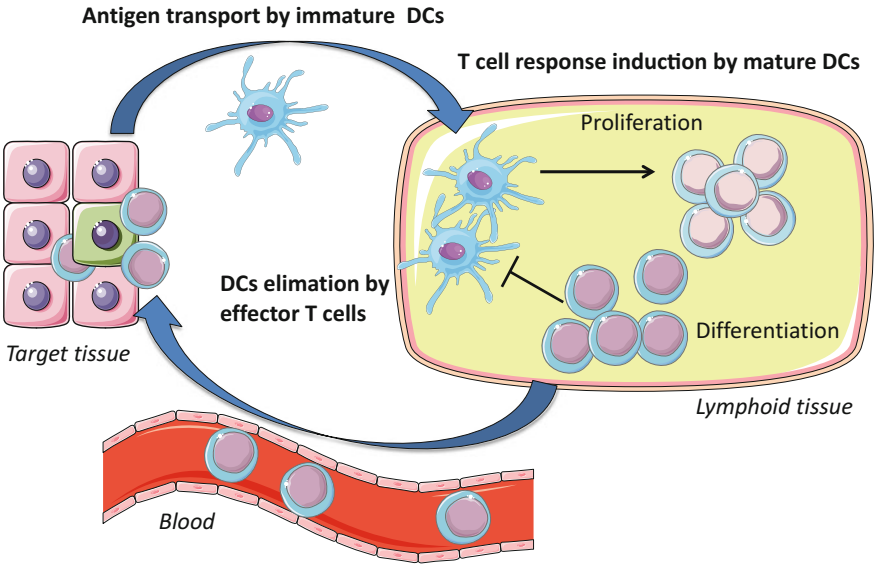


**Fig. 4.20** Compartmental scheme of systemic dynamics of adoptively transferred DC and CTL. Antigen-expressing DCs migrate from blood to spleen, where they induce clonal expansion of nave antigen-specific cytotoxic T-lymphocytes, whereas activated CTL eliminate DC. Arrows indicate the modelled processes. *Cell Pictures taken from Servier Medical Art*

**Table 4.7** Trafficking rates ($day^{-1}$) of $tet^+$ CTLs between Blood-, Spleen- and Liver compartments

| Organ | Blood | Spleen | Liver |
|---|---|---|---|
| Blood | $-1$ | $[0.012, 0.112]$ | 0.51 |
| Spleen | 0.022 | $-[0.012, 0.112]$ | 0 |
| Liver | 0.1 | 0 | $-0.51$ |

the spleen and equally applies to quiescent and activated CTL. The model predicts that 89% of peptide-specific CTL leave the blood compartment daily to organs other than the spleen and liver.

The sensitivity analysis of the model solutions suggests that T-cell receptor avidity, the half-life of DC, and the rate of CTL-mediated DC elimination are the major control parameters for optimal DC-induced CTL responses. For induction of high avidity CTLs, the number of adoptively transferred DC was of minor importance once a threshold of approximately 200 cells per spleen had been reached. As discussed before, the major objective of DC-based immunization is the maximal expansion and long-term maintenance of high numbers of antigen-specific T cells. Thus, the model can be applied to study the patterns of CTL population dynamics following repeated injection of H8-DC. Two sequential applications of $2 \times 10^4$ DCs at days 0, and 40 induce a robust CTL response with only a weak boosting effect. The

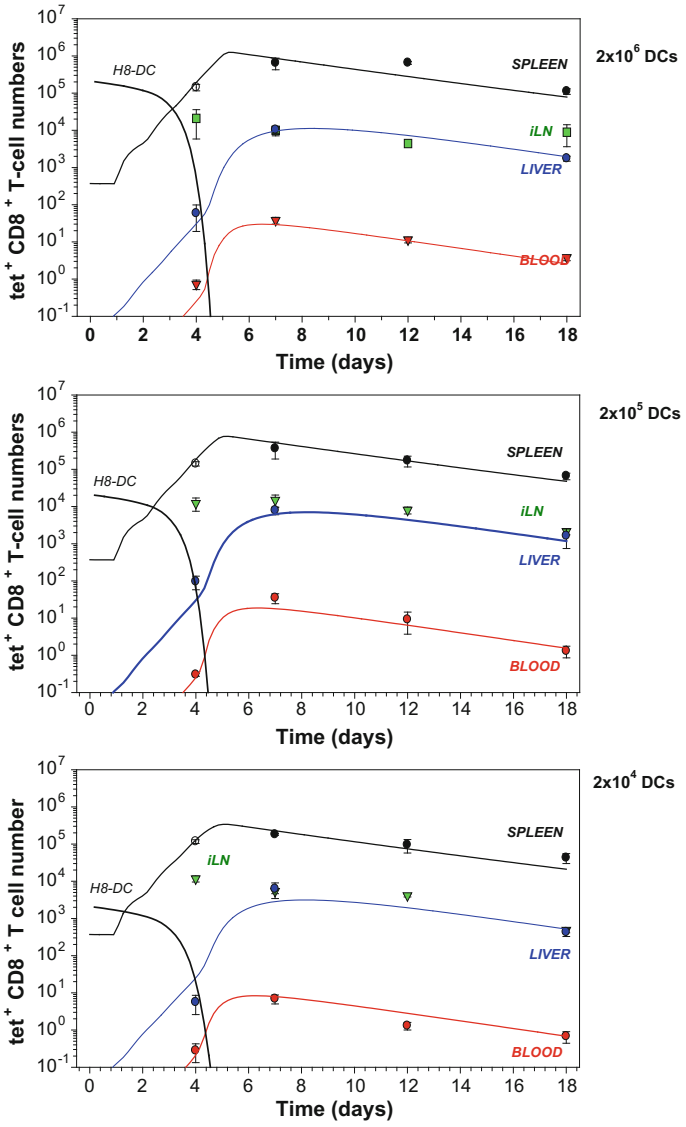


**Fig. 4.21** Compartmental dynamics of DC-induced tet$^+$ CTL responses in the spleen, blood and liver. The values for blood indicate the number of tet$^+CD8^+$ T cells/ml. The symbols represent averages of three mice $\pm$ SD

model predicts that as long as significant numbers of activated (or memory cells with a faster activation kinetics than that of naive) CTLs persist which ensure rapid elimination of antigen-expressing DCs, any further application of DCs has only a

limited enhancement effect. Nevertheless, such repeated DC application is apparently necessary to maintain high levels of activated CTLs.

## 4.4 MHV Infection: How Robust Is the IFN Type I-Mediated Protection?[6]

Human infections with highly virulent viruses, such as 1918 influenza or SARS-coronavirus, represent major threats to public health. The initial innate immune responses to such viruses have to restrict virus spread before the adaptive immune responses fully develop. Therefore, it is of fundamental practical importance to understand the robustness and fragility of the early protection against such virus infections mediated by the type I interferon response. The inherent complexity of the virus–host system suggests the application of mathematical modelling tools to predict the sensitivity of the kinetics and severity of infection to variations in virus and host parameters.

### *4.4.1 Immunobiology of MHV Infection*

The mouse hepatitis virus (MHV) infection represents a well- understood paradigmatic system for the analysis of type I IFN responses. MHV is a member of the Coronaviridae family that harbour a number of viruses causing severe diseases in animals and humans, such as acute hepatitis, encephalitis, infectious bronchitis, lethal infectious peritonitis and the severe acute respiratory syndrome (SARS) [74, 75]. In systemic MHV infection, spleen and liver represent major target organs [76], and primarily hematopoietic cell-derived type I IFN controls viral replication and virus-induced liver disease [77] as shown schematically in Fig. 4.22.

It has been demonstrated experimentally that pDCs are the major cell population generating IFN$\alpha$ during the initial phase of mouse coronavirus infection [76]. Importantly, mainly macrophages ($M\phi$) and, to a lesser extent conventional DCs, respond most efficiently to the pDC-derived type I IFN and thereby secure containment of MHV within secondary lymphoid organs (SLOs) [78]. Thus, the type I IFN-mediated crosstalk between pDCs and $M\phi$ represents an essential cellular pathway for the protection against MHV-induced liver disease. In systems biology terms, MHV infection triggers a complex array of processes at different biological scales such as protein expression, cellular migration or pathological organ damage. To focus on the front edge of the virus–host interaction, the modelling-based analysis specifically addresses the early dynamics (i.e. the first 48 h) of the type I IFN response to MHV since this is decisive for the outcome of the infection. The reductionists view of the most essential processes underlying the early systemic dynamics

[6] Material of this section uses the results Bocharov et al., PLoS Pathog. 6 (2010), e1001017.

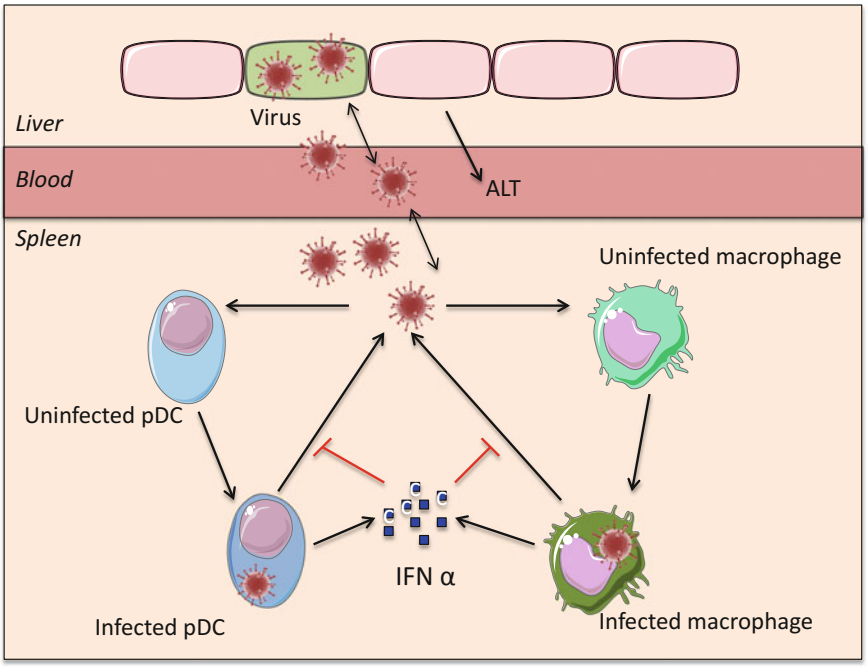


**Fig. 4.22** Scheme of type I IFN responses during cytopathic coronavirus infection. Systemic view of the processes determining the early kinetics of MHV infection. (The figure is adapted from Bocharov et al., PLoS pathogens, 2010). *Cell Pictures taken from Servier Medical Art*

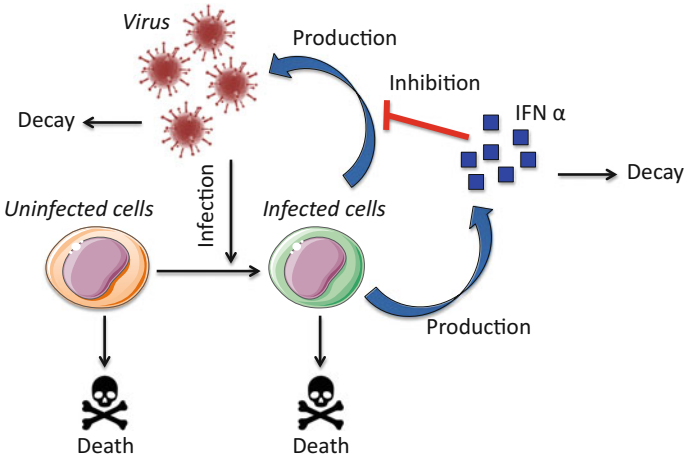


**Fig. 4.23** Basic module of mouse hepatitis virus infection and type I interferon response common for pDC and *Mϕ*. *Cell Pictures taken from Servier Medical Art*

of MHV infection, liver pathology and the first wave of type I IFN production is summarized in Figs. 4.22 and 4.23.

### 4.4.2 Setting up a Mathematical Model

To describe quantitatively the structure, dynamics and the operating principles that permit pDCs to initially shield the host against an overwhelming spread of the cytopathic MHV infection, one can follow a systems biology approach. First, the system dynamics is decomposed into a set of elementary, well-documented processes such as virus replication, target cell turnover and IFN-I decay, as well as the production of virus and IFN-I by infected cells (Fig. 4.22). This allows one to quantify the individual decay rates, the virus–target cell interaction parameters and the protective effect of IFN-I. Once these elementary modules of virus–target cell interactions were calibrated, one can use them as building blocks to set up an integrated mathematical model of pDC-mediated type I IFN responses against MHV infection in mice.

The mathematical model can be developed in stages by formulating and calibration the modules specifying

- Kinetics of virus, IFN-I and cells in vitro,
- Basic IFN-I response to infection of target cells,
- Compartmental dynamics of virus growth,
- Systemic model of MHV infection and IFN-I response.

The compartmental model considers the temporal dynamics of

- IFN-I $I(t)$ and unifected/infected pDCs and macrophages $C^{pDC}(t)$, $C^{M\phi}(t)$, $C_V^{pDC}(t)$, $C_V^{M\phi}(t)$ in spleen,
- systemic dynamics of the virus in spleen, blood and liver $V_S(t)$, $V_B(t)$, $V_L(t)$.
- dynamics of liver enzyme $AST$ in blood.

The corresponding equations formulated using a well-established approach (we refer to [3] for further details) read as follows:

$$\frac{dI}{dt}(t) = \rho_I^{pDC} C_V^{pDC}(t - \tau_I^{pDC}) + \rho_I^{M\phi} C_V^{M\phi}(t - \tau_I^{M\phi}) - d_I I(t) \tag{4.25}$$

$$\frac{dC_V^{pDC}}{dt}(t) = \sigma_V^{pDC} V_S(t) C^{pDC}(t) - d_{0CV}^{pDC} C_V^{pDC}(t) \tag{4.26}$$

$$\frac{dC_V^{M\phi}}{dt}(t) = \sigma_V^{M\phi} V_S(t) C^{M\phi}(t) - d_{0CV}^{M\phi} C_V^{M\phi}(t) \tag{4.27}$$

$$\frac{dC^{pDC}}{dt}(t) = -\sigma_V^{pDC} V_S(t) C^{pDC}(t) + d_{0C}^{pDC} \left( C_0^{pDC} - C^{pDC}(t) \right) \tag{4.28}$$

$$\frac{dC^{M\phi}}{dt}(t) = -\sigma_V^{M\phi} V_S(t) C^{M\phi}(t) + d_{0C}^{M\phi}\left(C_0^{M\phi} - C^{M\phi}(t)\right) \tag{4.29}$$

$$\begin{aligned}\frac{dV_S}{dt}(t) = &\frac{\rho_V^{pDC}}{1 + I(t)/\theta_{pDC}} C_V^{pDC}(t - \tau_V^{pDC}) + \frac{\rho_V^{M\phi}}{1 + I(t)/\theta_{M\phi}} C_V^{M\phi}(t - \tau_V^{M\phi}) \\ &- \left(\sigma_V^{pDC} C^{pDC}(t) + \sigma_V^{M\phi} C^{M\phi}(t)\right) V_S(t) - d_V V_S(t) \\ &- \mu_{SB} V_S(t) + \mu_{BS} V_B(t) \frac{Q_B}{Q_S}\end{aligned} \tag{4.30}$$

$$\frac{dV_B}{dt}(t) = \mu_{SB} V_S(t) \frac{Q_S}{Q_B} + \mu_{LB} V_L(t) \frac{Q_L}{Q_B} - (\mu_{BS} + \mu_{BL} + \mu_{BO})\, V_B(t) \tag{4.31}$$

$$\frac{dV_L}{dt}(t) = \beta_L V_L(t)\,(1 - V_L(t)/K_L) - \mu_{LB} V_L(t) + \mu_{BL} V_B(t) \frac{Q_B}{Q_L} \tag{4.32}$$

$$\frac{dA}{dt}(t) = \rho_A V_L(t) + d_A\left(A^* - A(t)\right). \tag{4.33}$$

The relevant information about the model parameters is summarized in Table 4.8. The best-fit solution is shown in Fig. 4.24.

### 4.4.3 Parameter Estimates and Sensitivity Analysis

The best-fit parameter estimates of the model characterize the concentration of IFN-I which is required to inhibit by twofold the production of virus by the infected cells. It appears that the pDC and M$\phi$ differ with respect to their sensitivity to the protective effect of interferon, so that the 50% reduction threshold concentrations are about 46 pg/ml and 1 pg/ml, respectively. The per capita type I IFN secretion rate also differs substantially between pDC and M$\phi$, being 15586 molec/h and 106 molec/h, respectively. The sensitivity analysis suggests a high protective capacity of single pDCs which protect $10^3$–$10^4$ $M\phi$ from cytopathic viral infection localized to spleen. The model allows one to determine the minimal protective unit of pre-activated pDCs in spleen to be around 200 cells which can rescue the host from severe disease. The modelling results suggest that the spleens capability to function as a sink for the virus produced in peripheral target organs remains operational as long as viral mutations do not permit accelerated growth in peripheral tissues.

**Table 4.8** Estimated parameters of the mathematical model MHV infection and type I IFN response

| Parameter | Biological meaning | Units | Best-fit estimate |
|---|---|---|---|
| $\rho_V^{DC}$ | Virus production rate by pDC | pfu/cell/h | 1.7 |
| $\rho_V^{M\phi}$ | Virus production rate by $M\phi$ | pfu/cell/h | 36.7 |
| $\rho_I^{DC}$ | Type I IFN production rate by pDC | pg/cell/h | $4.4 \times 10^{-4}$ |
| $\rho_I^{M\phi}$ | Type I IFN production rate by $M\phi$ | pg/cell/h | $1.0 \times 10^{-6}$ |
| $\theta_{pDC}$ | The threshold for 50% reduction of virus production rate by type I IFN | pg/ml | 45.8 |
| $\theta_{M\phi}$ | The threshold for 50% reduction of virus production rate by type I IFN | pg/ml | 0.97 |
| $\sigma_V^{DC}$ | Infection rate of pDC | cell/pfu/h | $1.3 \times 10^{-6}$ |
| $\sigma_V^{M\phi}$ | Infection rate of $M\phi$ | cell/pfu/h | $0.9 \times 10^{-7}$ |
| $\tau_V^{pDC}$ | Virus production delay by pDC | h | 5.96 |
| $\tau_V^{M\phi}$ | Virus production delay by pDC | h | 5.99 |
| $\tau_I^{pDC}$ | Type I IFN production delay by pDC | h | 5.77 |
| $\tau_I^{M\phi}$ | Type I IFN production delay by $M\phi$ | h | 5.8 |
| $d_{0CV}^{pDC}$, $k_{CV}^{pDC}$ | Gompertz death rate parameters for infected pDC | 1/h | 0.2, 0.087 |
| $d_{0CV}^{M\phi}$, $k_{CV}^{M\phi}$ | Gompertz death rate parameters for infected $M\phi$ | 1/h | 0.049, 0.057 |
| $\mu_{BS}$ | Virus transfer rate from blood to spleen | 1/h | 3.46 |
| $\mu_{BL}$ | Virus transfer rate from blood to liver | 1/h | 0.018 |
| $\mu_{SB}$ | Virus transfer rate from spleen to blood | 1/h | 0.91 |
| $\mu_{LB}$ | Virus transfer rate from liver to blood | 1/h | 0.61 |

(continued)

**Table 4.8** (continued)

| Parameter | Biological meaning | Units | Best-fit estimate |
|---|---|---|---|
| $\mu_{BO}$ | Virus elimination rate from blood | 1/h | 1.22 |
| $\beta_L$ | Virus growth rate in liver | pfu/ml/h | 0.78 |
| $K_L$ | Carrying capacity of the liver | pfu/ml | $10^7$ |
| $\rho_A$ | Rate constant of ALT release into blood | IU/l | $0.68 \times 10^{-3}$ |
| $d_A$ | Decay rate of ALT release in blood | 1/h | 0.16 |
| $A_*$ | Physiological level of ALT in blood | IU/l | 25 |

Importantly, the mathematical model of MHV infection can be used to evaluate the limits of protection against severe disease for increasing virus replication rates.

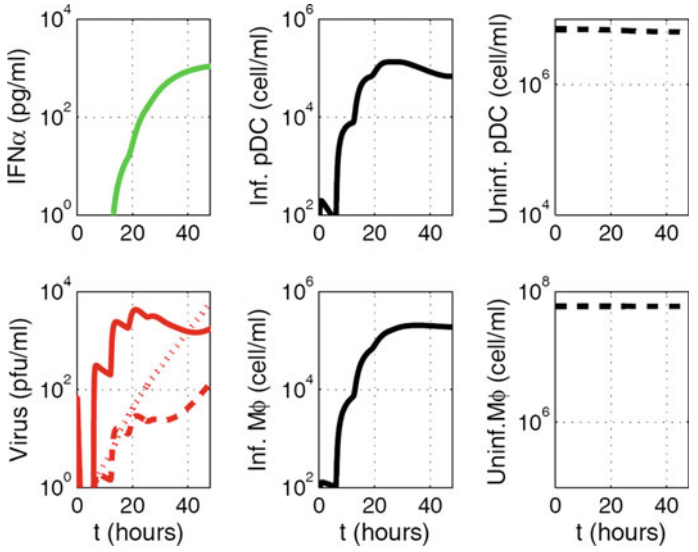


**Fig. 4.24** The solution of the compartmental model describing the kinetics of **a** interferon response and the population dynamics of **b** virus in spleen (solid line), liver (dotted line) and blood (dashed line), **c** and **e** uninfected/infected pDCs, **d** and **f** uninfected/infected macrophages. The parameters of the interferon response were estimated from in vitro and in vivo (spleen) data. The compartmental approach assumes an instantaneous mixing of IFN-I implying that the concentration across the SLO (spleen) is uniform. Reprinted from Mathematical Modelling of Natural Phenomena, Vol. 6, Bocharov et al., Reaction-Diffusion Modelling of Interferon Distribution in Secondary Lymphoid Organs, Pages 13–26, Copyright © 2011, with permission from EDP Sciences

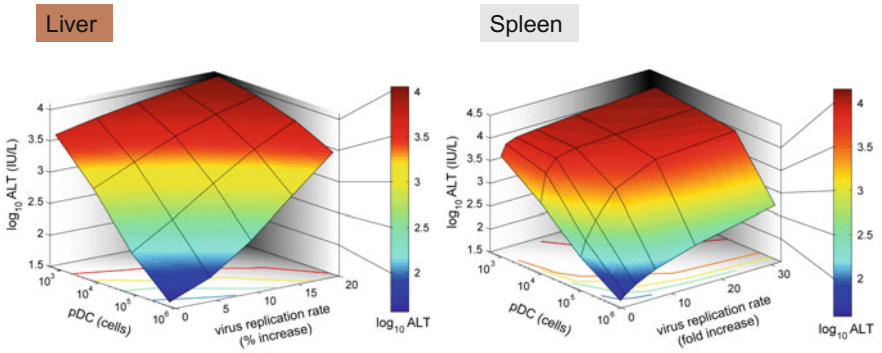


**Fig. 4.25** Effect of virus growth rates on pDC-mediated protection against disease. **a** Sensitivity of the disease severity to variations in pDC numbers (cells per spleen) and the global increase of viral replication rate in the liver (% increase). Disease severity is determined as peak ALT levels in serum within 48 h post-infection following i.v. infection with 50 pfu. **b** Determination of the systems robustness against disease with respect to variations in pDC numbers (cells per spleen) and increasing viral replication rates restricted to $M\phi$ in the spleen (Note: fold increase). (The figure is reprinted from Bocharov et al. PLoS pathogens, 2010)

Since various MHV strains display significant differences in their ability to replicate in different organs, two complementary scenarios were considered: the increase in virus growth rate in the peripheral organs (liver) versus secondary lymphoid organs (spleen). Figure 4.25 A shows that pDCs in spleen provide very limited protection against severe disease for faster replicating strains of the virus in hepatocytes. Indeed, only a 15% increase in the growth rate of MHV in the liver leads to infection with ALT levels rising to $10^3$ IU/L within 2 days. The decrease of pDC numbers in spleen makes the situation more fragile to even smaller increases in the virus growth rate. On the contrary, pDCs provide a robust protection against severe disease when the virulence-enhancing mutation leads to faster replication only in target cells located in spleen, i.e. splenic pDCs protect against severe disease for up to 30-fold increase in the viral replication rate in splenic $M\phi$ (See Fig. 4.25b). Taken together, these analyses indicate that the spleen represents a robust sink system able to cope with substantially enhanced virus production as long as this gain of viral fitness remains restricted to this SLO.

Overall, the modelling results suggest that the pDC population in spleen ensures a robust protection against virus variants which substantially downmodulate type I IFN secretion. However, the ability of pDCs to protect against severe disease caused by virus variants exhibiting an enhanced liver tropism and higher replication rates appears to be rather limited. Taken together, this system immunology analysis suggests that antiviral therapy against cytopathic viruses should primarily limit viral replication within peripheral target organs.

## 4.5 Identifying a Feedback Regulating Proliferation and Differentiation of CD4$^+$ T Cells[8]

In response to antigens, specific T-cell clones rapidly increase in size and then steeply decline, approaching relatively stable frequencies higher than those of the naive cell population. It was discovered by W.E. Paul's team (see data presented in [79]) that there is a log-linear relation between the CD4$^+$ T-cell precursor number (PN) and the factor of expansion (FE), with a slope of $\sim$0.5 over a range of 3–30,000 antigen-specific precursors per mouse. The experimental results suggested an inhibition mechanism of precursor expansion either by competition for specific antigen-presenting cells or by the action of other antigen-specific cells in the same microenvironment. Mathematical modelling can be used to identify the specific functions underlying the feedback regulation of the observed clonal dynamics.

As it was discussed in Chap. 2, the role of immunological theories in specifying mathematical models is essential. To formulate a mathematical model which describes and explains the observed findings, i.e. the data on CD4$^+$ T-cell expansion for various precursor numbers and the accompanying data sets from BrdU- and CFSE labeling kinetics, we considered the feedback-regulated balance of growth and differentiation concept by Grossman and Paul [80–82]. It was assumed that the most differentiated effectors (or memory cells) limit the growth of less differentiated effectors, locally, by increasing the rate of differentiation of the latter cells in a dose-dependent manner [4]. The biological scheme and the sequence of functionally distinct stages in cell development underlying the equations of the mathematical model is shown schematically in Fig. 4.26. Cell proliferation and differentiation rates were assumed to be regulated in a feedback fashion, i.e. they depend on the number of differentiated cells.

The population dynamics of the above four subsets of CD4$^+$ T cells was modelled using a system of ODEs. The core mathematical model was used for data assimilation either directly (data on the kinetics of clonal expansion and contraction) or in two extended forms in which the cell subsets were further subdivided into unlabelled and labelled compartments, to describe the BrdU-labeling data and CFSE dilution data, respectively. A number of data fitting and analysis methods, including the maximum likelihood approach, Akaike information criteria, statistical model comparison methods and sensitivity analyses were used to identify a parsimonious model of the kinetics of antigen-driven CD4$^+$ T-cell expansion (we refer to [4] for details). The set of core model equations with feedback regulation is represented in the following form:

$$\frac{\mathrm{d}}{\mathrm{d}t}X_1(t) = p_1 X_1(t) - \left(\alpha_1 + \alpha_{12}\frac{1}{1 + (Z_1(t) + Z_2(t))/\theta_{x1}}Z_2\right)X_1, \qquad (4.34)$$

[8]Material of this subsection uses the results of our studies from Proceedings of the National Academy of Sciences of the United States of America (PNAS USA), Vol. 108, Bocharov et al., Feedback regulation of proliferation vs. differentiation rates explains the dependence of CD4 T-cell expansion on precursor number, Pages 3318–3323, Copyright © 2011 with permission from PNAS USA.

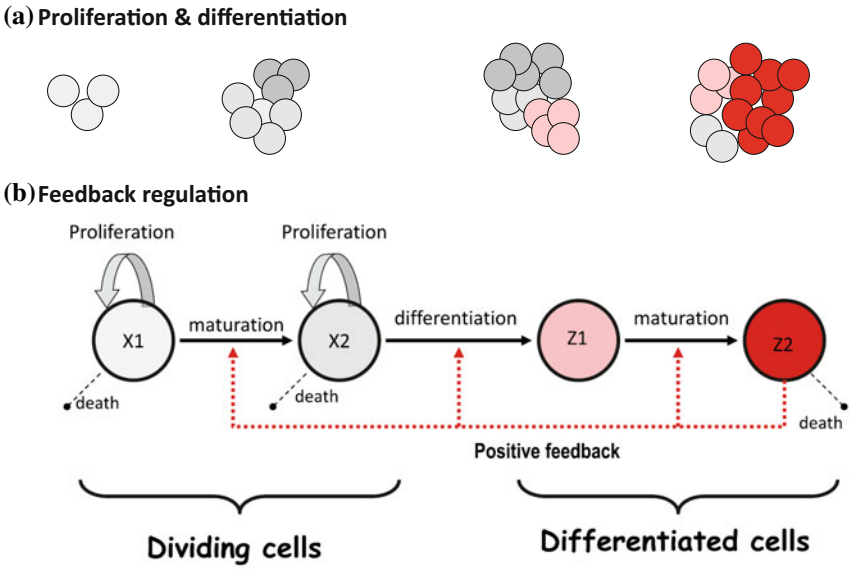


**Fig. 4.26** Biological scheme of the concept of feedback-regulated balance of growth and differentiation of cells by Z. Grossman by W. Paul. **a** Heterogeneity of the proliferation and differentiating clones. **b** A simple view of the sequence of functionally distinct stages in cell development. Cell proliferation and differentiation rates are assumed to be regulated in a feedback fashion, i.e. they depend on the number of differentiated cells. Two subsets X1 and X2 represent the proliferating cell population. X1 is less mature than X2. The differentiated cell populations Z1 and Z2 can not divide. The population of more differentiated cells Z2 controls the balance of proliferation and differentiation of X1 and X2 subsets. Reprinted from Proceedings of the National Academy of Sciences of the United States of America (PNAS USA), Vol. 108, Quiel et al., Antigen-stimulated CD4 T-cell expansion is inversely and log-linearly related to precursor number, Pages 3312–3317, Copyright © 2011 with permission from PNAS USA

$$\frac{\mathrm{d}}{\mathrm{d}t}X_2(t) = p_2 X_2(t) + \left(\alpha_1 + \alpha_{12}\frac{1}{1+(Z_1(t)+Z_2(t))/\theta_{x1}}Z_2\right)X_1 - (\alpha_2 + \alpha_{22}Z_2)\,X_2, \quad (4.35)$$

$$\frac{\mathrm{d}}{\mathrm{d}t}Z_1(t) = (\alpha_2 + \alpha_{22}Z_2)\,X_2 - \beta_1 Z_1, \quad (4.36)$$

$$\frac{\mathrm{d}}{\mathrm{d}t}Z_2(t) = \beta_1 Z_1 - \delta Z_2. \quad (4.37)$$

The consistency of the model with data on clonal expansion of $CD4^+$ T cells starting from 300 precursors in the LNs at the time of immunization and $3 \times 10^4$ cells along with the evolving structure of the clones is illustrated in Fig. 4.27. The model gives a precise quantitative relation between the factor of expansion ($FE$) and the precursor number ($PN$) as follows: $FE = PN^{0.48} \times 3.981$.

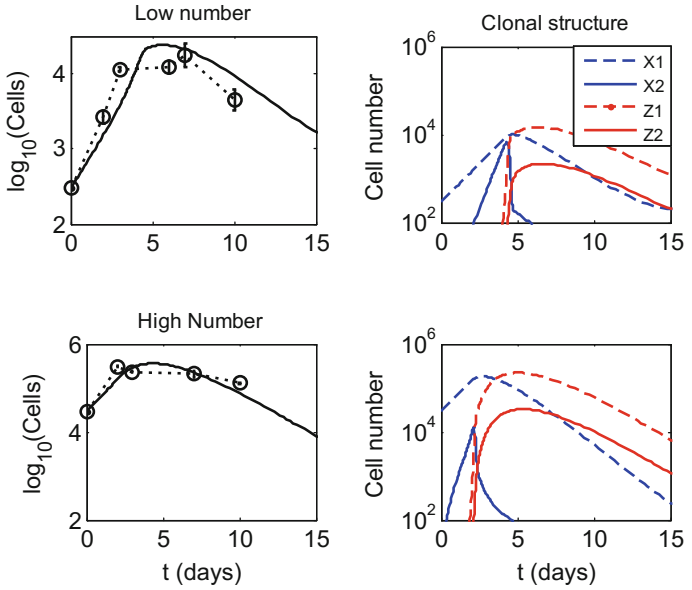


**Fig. 4.27** Model-based data assimilation and parameter estimation. The kinetics of clonal expansion and contraction for different initial numbers of transferred antigen-specific precursor $CD4^+$ T cells. The time evolution of the total number of cells (Left) and evolution of the clonal structure (Right) are shown. Upper row, 300 antigen-specific $CD4^+$ T cells in the LNs at the time of immunization; Lower row, $3 \times 10^4$ antigen-specific precursor $CD4^+$ T cells at immunization. Reprinted from Proceedings of the National Academy of Sciences of the United States of America (PNAS USA), Vol. 108, Bocharov et al., Feedback regulation of proliferation vs. differentiation rates explains the dependence of CD4 T-cell expansion on precursor number, Pages 3318–3323, Copyright © 2011 with permission from PNAS USA

One can conclude that the feedback-regulated balance of growth and differentiation hypothesis, although requiring definite experimental characterization of the hypothetical cell phenotypes and molecules involved in the identified regulation, can explain the kinetics of $CD4^+$ T-cell responses to antigenic stimulation. We note that a mathematical model based on a different hypothesis (e.g. 'grazing of peptide-MHC complexes') was proposed to explain the same phenomenon although in a semi-quantitative manner [83]. However, no evidence of its consistency with all available data sets that were described and analysed in [4, 79] was presented.

In conclusion, while a multitude of mathematical models can be generated to describe any given immunological phenomenon, it is crucial to always link it to available experimental data. If model and data are in good agreement, then the model may help to generate new hypothesis of underlying mechanisms and provide further testable predictions. In addition, as outlined in Sect. 4.5, a model may also strongly support a novel hypothesis that was brought up ad hoc from immunological considerations.

## References


1. Bocharov, G.A. Modelling the dynamics of LCMV infection in mice: conventional and exhaustive CTL responses. *J. Theor. Biol.*, **192** (1998) 283–308.
2. Luzyanina T, Engelborghs K, Ehl S, Klenerman P, Bocharov G. Low level viral persistence after infection with LCMV: a quantitative insight through numerical bifurcation analysis. Math Biosci. 2001 ;173(1):1–23.
3. Bocharov G, Zst R, Cervantes-Barragan L, Luzyanina T, Chiglintsev E, Chereshnev VA, Thiel V, Ludewig B. A systems immunology approach to plasmacytoid dendritic cell function in cytopathic virus infections. PLoS Pathog. 2010 ;6(7):e1001017.
4. Bocharov G, Quiel J, Luzyanina T, Alon H, Chiglintsev E, Chereshnev V, Meier-Schellersheim M, Paul WE, Grossman Z. Feedback regulation of proliferation vs. differentiation rates explains the dependence of CD4 T-cell expansion on precursor number. Proc Natl Acad Sci U S A. 2011 ;108(8):3318–3323
5. Doherty PC, Zinkernagel RM: H-2 compatibility is required for T-cell-mediated lysis of target cells infected with lymphocytic choriomeningitis virus. J Exp Med 1975, 141:502–507.
6. Zinkernagel RM, Doherty PC: Restriction of in vitro T cell-mediated cytotoxicity in lymphocytic choriomeningitis within a syngeneic or semiallogeneic system. Nature 1974, 248:701–702.
7. Kagi D, Ledermann B, Burki K, Seiler P, Odermatt B, Olsen KJ, Podack ER, Zinkernagel RM, Hengartner H: Cytotoxicity mediated by T cells and natural killer cells is greatly impaired in perforin-deficient mice. Nature 1994, 369:31–37.
8. Masson D, Tschopp J: Isolation of a lytic, pore-forming protein (perforin) from cytolytic T-lymphocytes. J Biol Chem 1985, 260:9069–9072.
9. Ehl S, Klenerman P, Zinkernagel RM, Bocharov G: The impact of variation in the number of CD8(+) T-cell precursors on the outcome of virus infection. Cell Immunol 1998, 189:67–73.
10. Waggoner SN, Cornberg M, Selin LK, Welsh RM: Natural killer cells act as rheostats modulating antiviral T cells. Nature 2012, 481:394–398.
11. Karrer U, Althage A, Odermatt B, Roberts CW, Korsmeyer SJ, Miyawaki S, Hengartner H, Zinkernagel RM: On the key role of secondary lymphoid organs in antiviral immune responses studied in alymphoplastic (aly/aly) and spleenless (Hox11(-)/-) mutant mice. J Exp Med 1997, 185:2157–2170.
12. Cole GA, Nathanson N, Prendergast RA: Requirement for theta-bearing cells in lymphocytic choriomeningitis virus-induced central nervous system disease. Nature 1972, 238:335–337.
13. Kim JV, Kang SS, Dustin ML, McGavern DB: Myelomonocytic cell recruitment causes fatal CNS vascular injury during acute viral meningitis. Nature 2009, 457:191–195.
14. Riviere Y, Gresser I, Guillon JC, Tovey MG: Inhibition by anti-interferon serum of lymphocytic choriomeningitis virus disease in suckling mice. Proc Natl Acad Sci U S A 1977, 74:2135–2139.
15. Chen HD, Fraire AE, Joris I, Brehm MA, Welsh RM, Selin LK: Memory CD8+ T cells in heterologous antiviral immunity and immunopathology in the lung. Nat Immunol 2001, 2:1067–1076.
16. Ohashi PS, Oehen S, Buerki K, Pircher H, Ohashi CT, Odermatt B, Malissen B, Zinkernagel RM, Hengartner H: Ablation of "tolerance" and induction of diabetes by virus infection in viral antigen transgenic mice. Cell 1991, 65:305–317.
17. Oldstone MB, Nerenberg M, Southern P, Price J, Lewicki H: Virus infection triggers insulin-dependent diabetes mellitus in a transgenic model: role of anti-self (virus) immune response. Cell 1991, 65:319–331.
18. Barber DL, Wherry EJ, Masopust D, Zhu B, Allison JP, Sharpe AH, Freeman GJ, Ahmed R: Restoring function in exhausted CD8 T cells during chronic viral infection. Nature 2006, 439:682–687.
19. Moskophidis D, Lechner F, Pircher H, Zinkernagel RM: Virus persistence in acutely infected immunocompetent mice by exhaustion of antiviral cytotoxic effector T cells. Nature 1993, 362:758–761.

20. Wherry EJ, Ha SJ, Kaech SM, Haining WN, Sarkar S, Kalia V, Subramaniam S, Blattman JN, Barber DL, Ahmed R: Molecular signature of CD8+ T cell exhaustion during chronic viral infection. Immunity 2007, 27:670–684.
21. Zajac AJ, Blattman JN, Murali-Krishna K, Sourdive DJ, Suresh M, Altman JD, Ahmed R: Viral immune evasion due to persistence of activated T cells without effector function. J Exp Med 1998, 188:2205–2213.
22. Leavy O: Tumour immunology: A triple blow for cancer. Nat Rev Immunol 2015, 15:265.
23. Trautmann L, Janbazian L, Chomont N, Said EA, Gimmig S, Bessette B, Boulassel MR, Delwart E, Sepulveda H, Balderas RS, et al: Upregulation of PD-1 expression on HIV-specific CD8+ T cells leads to reversible immune dysfunction. Nat Med 2006, 12:1198–1202.
24. Velu V, Titanji K, Zhu B, Husain S, Pladevega A, Lai L, Vanderford TH, Chennareddi L, Silvestri G, Freeman GJ, et al: Enhancing SIV-specific immunity in vivo by PD-1 blockade. Nature 2009, 458:206–210.
25. Moskophidis D, Lechner F, Pircher H, Zinkernagel RM. Virus persistence in acutely infected immunocompetent mice by exhaustion of antiviral cytotoxic effector T cells. Nature. 1993;362(6422):758–761
26. Wherry EJ, Kurachi M: Molecular and cellular insights into T cell exhaustion. Nat Rev Immunol 2015, 15:486–499.
27. A. Ciurea, P. Klenerman, L. Hunziker, E. Horvath, B. Odermatt, A. F. Ochsenbein, H. Hengartner, and R. M. Zinkernagel. Persistence of lymphocytic choriomeningitis virus at very low levels in immune mice. *Proc. Natl. Acad. Sci. USA*, 96:11964–11969, 1999.
28. A. J. Zajac, J. N. Blattman, K. Murali-Krishna, D. J. D. Sourdive, M. Suresh, J. D. Altman, and R. Ahmed. Viral immune evasion due to persistence of activated T cells without effector function. *J. Exp. Med.*, 188:2205–2213, 1998.
29. R. Ahmed, L. A. Morrison, and D. M. Knipe. Viral persistence. In N. Nathanson et al., editor, *Viral Pathogenesis*, pages 181–205. Lippincott-Raven Publishers, Philadelphia, 1997.
30. M. B. A. Oldstone. Viral persistence. *Cell*, 56:517–520, 1989.
31. D. Tortorella, B. E. Gewurz, M. H. Furman, D. J. Schust, and H. L. Ploegh. Viral subversion of the immune system. *Ann. Rev. Immunol.*, 18:861–926, 2000.
32. R. Ahmed, B. D. Jamieson, and D. D. Porter. Immune therapy of a persistent and disseminated viral infection. *J. Virol.*, 61:3920–3929, 1987.
33. O. Planz, S. Ehl, E. Furrer, E. Horvath, M.-A. Bründler, H. Hengartner, and R. M. Zinkernagel. A critical role of neutralizing-antibody-producing B cells, $CD4^+$ T cells and interferons in persistent and acute infections of mice with lymphocytic choriomeningitis virus: Implications for adoptive immunotherapy of virus carriers. *Proc. Natl. Acad. Sci. USA*, 94:6874–6879, 1997.
34. K. Engelborghs. *DDE-BIFTOOL: a Matlab package for bifurcation analysis of delay differential equations*. Department of Computer Science, Katholieke Universiteit Leuven, Belgium, March 2000. Report TW 305, (http://www.cs.kuleuven.ac.be/~koen/delay/ddebiftool.shtml).
35. K. Engelborghs. *Numerical bifurcation analysis of delay differential equations*. Ph.D. thesis, Department of Computer Science, Katholieke Universiteit Leuven, Belgium, 2000.
36. K. Engelborghs and D. Roose. On stability of LMS methods and characteristic roots of delay differential equations. Submitted, 2000.
37. K. Engelborghs and E. J. Doedel. Stability of piecewise polynomial collocation methods for computing periodic solutions of delay differential equations. Submitted, 2000.
38. K. Engelborghs, T. Luzyanina, K. in't Hout, and D. Roose. Collocation methods for the computation of periodic solutions of delay differential equations. *SIAM J. Sci. Comput.*, 22:1593–1609, 2000.
39. F. Lehmann-Grube. *Lymphocytic Choriomeningitis Virus*. New York:Springer-Verlag, 1971.
40. Mims, C.A. (1995). Mims Pathogenesis of Infectious Disease. London: Academic Press.
41. Zinkernagel, R.M. and Hengartner H. (1997). Antiviral immunity. Immunol. Today 18, 258–260.
42. Kägi, D., Odermatt, B., Seiler, P., Zinkernagel, R. M., Mak, T.W. Hengartner, H. (1997). Reduced incidence and delayed onset of diabetis in perforindeficient nonobese diabetic mice. J. Exp. Med. 186, 989–997.

43. Ludewig, B., Odermatt, B., Landmann, S. Hengartner, H. and Zinkernagel, R.M. (1998). Dendritic cells induce autoimmune diabetis and maintain disease via de novo formation of local lymphoid tissue. J. Exp. Med. 188, 1–9.
44. Binder, D., van den Broek, M. F., Kägi, D., Bluethmann, Fehr, J., Hengartner, H. and Zinkernagel, R.M. (1998). Aplastic anemia rescued by exhaustion of cytokine-secreting CD8+ T cells in persistent infection with lymphocytic choriomeningitis virus. J. Exp. Med. 187, 1903–1920
45. Oldstone, M.B.A., Blount, P., Southern, P.J. and Lampert, P.W. (1986). Cytoimmunotherapy for persistent virus infection reveals a unique clearance pattern from the central nervous system. Nature, 321, 239–243.
46. Zinkernagel, R.M. (1993). Immunity to viruses. In: Fundamental Immunology, 3rd. Edn. (Paul, W., ed.), Chap. 34, pp. 1211–1250. New York: Raven Press.
47. Zinkernagel, R.M., Haenseler, E., Leist, T., Cerny, A., Hengartner, H. and Althage, A. (1986). T cell-mediated hepatitis in mice infected with lymphocytic choriomeningitis virus. J. Exp. Med. 164, 1075–1092.
48. Zinkernagel, R.M., Planz, O., Ehl, S., Battegay, M., Odermatt, B., Klenerman, P. and Hengartner, H. (1999). General and specific immunosuppression caused by antiviral T-cell responses. Immunol. Reviews 168,305–315.
49. Odermatt, B., Eppler, M., Leist, T.P., Hengartner, H. and Zinkernagel, R.M. (1991) Virus-triggered acquired immunodeficiency by cytotoxic T-cell-dependent destruction of antigen-presenting cells and lymph node follicle structure. Proc. Natl. Acad. Sci. USA, 88, 8252–8256.
50. Jacquez, J.A. and Simon, C.P. (1993). Qualitative theory of compartmental systems. SIAM Review, 35, 43–79.
51. Bocharov G, Klenerman P, Ehl S. Modelling the dynamics of LCMV infection in mice: II. Compartmental structure and immunopathology. J Theor Biol. 2003 Apr 7;221(3):349–378. Erratum in: J Theor Biol. 2004 Jan 7;226(1):123
52. Pardoll, D. M., Spinning molecular immunology into successful immunotherapy. Nat. Rev. Immunol. 2002. 2: 227–238.
53. Steinman, R. M. and Pope, M., Exploiting dendritic cells to improve vaccine efficacy. J. Clin. Invest 2002. 109: 1519–1526.
54. Schuler, G., Schuler-Thurner, B. and Steinman, R. M., The use of dendritic cells in cancer immunotherapy. Curr. Opin. Immunol. 2003. 15: 138–147.
55. Ludewig, B., Ehl, S., Karrer, U., Odermatt, B., Hengartner, H. and Zinkernagel, R. M., Dendritic cells efficiently induce protective antiviral immunity. J. Virol. 1998. 72: 3812–3818.
56. Ludewig, B., Ochsenbein, A. F., Odermatt, B., Paulin, D., Hengartner, H. and Zinkernagel, R. M., Immunotherapy with dendritic cells directed against tumor antigens shared with normal host cells results in severe autoimmune disease. J. Exp. Med. 2000. 191: 795–804.
57. Ludewig, B., Barchiesi, F., Pericin, M., Zinkernagel, R. M., Hengartner, H. and Schwendener, R. A., In vivo antigen loading and activation of dendritic cells via a liposomal peptide vaccine mediates protective antiviral and anti-tumour immunity. Vaccine 2000. 19: 23–32.
58. Nair, S. K., Boczkowski, D., Morse, M., Cumming, R. I., Lyerly, H. K. and Gilboa, E., Induction of primary carcinoembryonic antigen (CEA)-specific cytotoxic T lymphocytes in vitro using human dendritic cells transfected with RNA. Nat. Biotechnol. 1998. 16: 364–369.
59. Rea, D., Havenga, M. J., van Den Assem, M., Sutmuller, R. P., Lemckert, A., Hoeben, R. C., Bout, A., Melief, C. J. and Offringa, R., Highly efficient transduction of human monocyte-derived dendritic cells with subgroup B fiber-modified adenovirus vectors enhances transgene-encoded antigen presentation to cytotoxic T cells. J. Immunol. 2001. 166: 5236–5244.
60. Hsu, F. J., Benike, C., Fagnoni, F., Liles, T. M., Czerwinski, D., Taidi, B., Engleman, E. G. and Levy, R., Vaccination of patients with B cell lymphoma using autologous antigen-pulsed dendritic cells. Nat. Med. 1996. 2: 52–58.
61. Nestle, F. O., Alijagic, S., Gilliet, M., Sun, Y., Grabbe, S., Dummer, R., Burg, G. and Schadendorf, D., Vaccination of melanoma patients with peptide- or tumor lysate-pulsed dendritic cells. Nat. Med. 1998. 4: 328–332.
62. Fong, L. and Engleman, E. G., Dendritic cells in cancer immunotherapy. Annu. Rev. Immunol. 2000. 18: 245–273.

63. Ludewig, B., Bonilla, W. V., Dumrese, T., Odermatt, B., Zinkernagel, R. M. and Hengartner, H., Perforin-independent regulation of dendritic cell homeostasis by CD8(+) T cells in vivo: implications for adaptive immunotherapy. Eur. J. Immunol. 2001. 31: 1772–1779.
64. Ludewig, B., Oehen, S., Barchiesi, F., Schwendener, R. A., Hengartner, H. and Zinkernagel, R. M., Protective antiviral cytotoxic T cell memory is most efficiently maintained by restimulation via dendritic cells. J. Immunol. 1999. 163: 1839–1844.
65. Dunn, G. P., Bruce, A. T., Ikeda, H., Old, L. J. and Schreiber, R. D., Cancer immunoediting: from immunosurveillance to tumor escape. Nat. Immunol. 2002. 3: 991–998.
66. Brossart, P., Zobywalski, A., Grunebach, F., Behnke, L., Stuhler, G., Reichardt, V. L., Kanz, L. and Brugger, W., Tumor necrosis factor alpha and CD40 ligand antagonize the inhibitory effects of interleukin 10 on T cell stimulatory capacity of dendritic cells. Cancer Res. 2000. 60: 4485–4492.
67. De Boer, R. J. and Perelson, A. S., Towards a general function describing T cell proliferation. J. Theor. Biol. 1995. 175: 567–576.
68. Borghans, J. A., Taams, L. S., Wauben, M. H. and De Boer, R. J., Competition for antigenic sites during T cell proliferation: a mathematical interpretation of in vitro data. Proc. Natl. Acad. Sci. USA 1999. 96: 10782–10787.
69. Ronchese, F. and Hermans, I. F., Killing of dendritic cells: a life cut short or a purposeful death? J. Exp. Med. 2001. 194: F23–F26.
70. Ludewig, B., Krebs, P., Junt, T. and Bocharov, G., Dendritic cell homeostasis in the regulation of self-reactivity. Curr. Pharm. Des. 2003. 9: 221–231.
71. Perelson, A. S., Modelling viral and immune system dynamics. Nat. Rev. Immunol. 2002. 2: 28–36.
72. Chakraborty, A. K., Dustin, M. L. and Shaw, A. S., In silico models for cellular and molecular immunology: successes, promises and challenges. Nat. Immunol. 2003. 4: 933–936.
73. Komarova, N. L., Barnes, E., Klenerman, P. and Wodarz, D., Boosting immunity by antiviral drug therapy: a simple relationship among timing, efficacy, and success. Proc. Natl. Acad. Sci. USA 2003. 100: 1855–1860.
74. Barchet W, Cella M, Colonna M (2005) Plasmacytoid dendritic cellsvirus experts of innate immunity. Semin Immunol 17: 253–261.
75. Perlman S, Netland J (2009) Coronaviruses post-SARS: update on replication and pathogenesis. Nat Rev Microbiol 7: 439–450.
76. Cervantes-Barragan L, Zust R, Weber F, Spiegel M, Lang KS, et al. (2007) Control of coronavirus infection through plasmacytoid dendritic-cell-derived type I interferon. Blood 109: 1131–1137.
77. Lang PA, Cervantes-Barragan L, Verschoor A, Navarini AA, Recher M, et al. (2009) Hematopoietic cell-derived interferon controls viral replication and virusinduced disease. Blood 113: 1045–1052.
78. Cervantes-Barragan L, Kalinke U, Zust R, Konig M, Reizis B, et al. (2009) Type I IFN-mediated protection of macrophages and dendritic cells secures control of murine coronavirus infection. J Immunol 182: 1099–1106.
79. Quiel J, Caucheteux S, Laurence A, Singh NJ, Bocharov G, Ben-Sasson SZ, Grossman Z, Paul WE. Antigen-stimulated CD4 T-cell expansion is inversely and log-linearly related to precursor number. Proc Natl Acad Sci U S A. 2011 ;108(8):3312–3317
80. Grossman Z, Paul WE: Dynamic tuning of lymphocytes: physiological basis, mechanisms, and function. Annu Rev Immunol 2015, 33:677–713.
81. Grossman, Z., Min, B., Meier-Schellersheim, M. and Paul, W. E., Concomitant regulation of T cell activation and homeostasis. Nat. Rev. Immunol. 2004. 4: 7–15.
82. Grossman Z. Recognition of self and regulation of specificity at the level of cell populations. Immunol Rev (1984) 79:119–138.

83. De Boer RJ, Perelson AS. Antigen-stimulated CD4 T cell expansion can be limited by their grazing of peptide-MHC complexes. J Immunol. 2013 Jun 1;190(11):5454–5458. https://doi.org/10.4049/jimmunol.1203569.
84. Ludewig B, Krebs P, Junt T, Metters H, Ford NJ, Anderson RM, Bocharov G. Determining control parameters for dendritic cell-cytotoxic T lymphocyte interaction. Eur J Immunol. 2004;34(9):2407–2418.